



Review

GNSS Reflectometry-Based Ocean Altimetry: State of the Art and Future Trends

Tianhe Xu ¹, Nazi Wang ^{1,*}, Yunqiao He ¹, Yunwei Li ¹, Xinyue Meng ¹, Fan Gao ¹ and Ernesto Lopez-Baeza ²

¹ Institute of Space Sciences, Shandong University, Weihai 264209, China; thxu@sdu.edu.cn (T.X.); heyunqiao@mail.sdu.edu.cn (Y.H.); yunweili@email.sdu.edu.cn (Y.L.); mengxinyue@mail.sdu.edu.cn (X.M.); gaofan@sdu.edu.cn (F.G.)

² Faculty of Physics, University of Valencia, 46001 Valencia, Spain; ernesto.lopez@uv.es

* Correspondence: wnz@sdu.edu.cn; Tel.: +86-063-1562-1748

Abstract: For the past 20 years, Global Navigation Satellite System reflectometry (GNSS-R) technology has successfully shown its potential for remote sensing of the Earth's surface, including ocean and land surfaces. It is a multistatic radar that uses the GNSS signals reflected from the Earth's surface to extract land and ocean characteristics. Because of its numerous advantages such as low cost, multiple signal sources, and all-day/weather and high-spatiotemporal-resolution observations, this new technology has attracted the attention of many researchers. One of its most promising applications is GNSS-R ocean altimetry, which can complement existing techniques such as tide gauging and radar satellite altimetry. Since this technology for ocean altimetry was first proposed in 1993, increasing progress has been made including diverse methods for processing reflected signals (such as GNSS interferometric reflectometry, conventional GNSS-R, and interferometric GNSS-R), different instruments (such as an RHCP antenna with one geodetic receiver, a linearly polarized antenna, and a system of simultaneously used RHCP and LHCP antennas with a dedicated receiver), and different platform applications (such as ground-based, air-borne, or space-borne). The development of multi-mode and multi-frequency GNSS, especially for constructing the Chinese BeiDou Global Navigation Satellite System (BDS-3), has enabled more free signals to be used to further promote GNSS-R applications. The GNSS has evolved from its initial use of GPS L1 and L2 signals to include other GNSS bands and multi-GNSS signals. Using more advanced, multi-frequency, and multi-mode signals will bring new opportunities to develop GNSS-R technology. In this paper, studies of GNSS-R altimetry are reviewed from four perspectives: (1) classifications according to different data processing methods, (2) different platforms, (3) development of different receivers, and (4) our work. We overview the current status of GNSS-R altimetry and describe its fundamental principles, experiments, recent applications to ocean altimetry, and future directions.

Keywords: GNSS-R; ocean altimetry; sea level; receiver



Citation: Xu, T.; Wang, N.; He, Y.; Li, Y.; Meng, X.; Gao, F.; Lopez-Baeza, E. GNSS Reflectometry-Based Ocean Altimetry: State of the Art and Future Trends. *Remote Sens.* **2024**, *16*, 1754. <https://doi.org/10.3390/rs16101754>

Academic Editors: Andrés Calabia, Xuerui Wu, Xinggang Zhang and Kousuke Heki

Received: 19 April 2024

Revised: 8 May 2024

Accepted: 14 May 2024

Published: 15 May 2024



Copyright: © 2024 by the authors. Licensee MDPI, Basel, Switzerland. This article is an open access article distributed under the terms and conditions of the Creative Commons Attribution (CC BY) license (<https://creativecommons.org/licenses/by/4.0/>).

1. Introduction

Sea level monitoring plays an important role in global climate analysis, water conservancy projects, hydrological forecasting and planning, disaster monitoring, marine transportation, and safety measures for people living in coastal regions [1]. The rise in global mean sea levels with global warming threatens coastal populations and ecosystems. Thus, it is greatly important to monitor the sea level.

Pressure and acoustic tide gauges (TGs) and radar altimeters are traditionally used to monitor long-time and large-scale global sea level variations. They have their respective advantages and disadvantages. TGs can provide observations over a long time with a high sampling rate and high precision but only in situ and relative to different sea levels. Conventional TG measurements also suffer from long-time variations due to vertical surface motion [2]. Therefore, more tide gauges have been collocated with a Global Navigation

Satellite System (GNSS) receiver to use its data to correct this vertical motion and provide absolute sea level variation. Meanwhile, TGs require direct contact with the water, and they are vulnerable to water corrosion, thus requiring regular maintenance. Radar altimetry can provide absolute sea level variation over the open sea, but it has a low sampling rate and a long revisit period, and the contamination of radar signals by land reduces the precision of coastal sea level observations [3] (pp. 297–330). Its spatial and temporal resolutions cannot meet the requirements for detecting the mesoscale features of ocean surface variation, such as swell and waves [4]. In coastal areas especially, the precision of sea level retrieval from radar altimetry is poor.

The initial aim in developing GNSS was to realize positioning, navigation, and timing (PNT). The development of GNSS-R provides a new and promising alternative approach to ocean and land remote sensing such as sea level monitoring [2,5], sea surface wind retrieval [6,7], snow depth determination [8,9], and soil moisture estimation [10,11]. The fundamental principle of GNSS-R is that the strength, phase, and polarization of GNSS signals change after they are reflected from a land or ocean surface, and the characteristics of the reflection surface can be deduced from these changes. Because GNSS continuously broadcasts multi-constellation and multi-frequency L-band signals in all-day and all-weather conditions, it can take measurements along several reflection tracks from different GNSS transmitters in parallel. This provides exceptional observations all the time and through all types of weather with high spatiotemporal sampling and rapid revisit time over the Earth surfaces. GNSS-R requires only the receiver component of traditional remote sensing, such as satellite radar. This significantly reduces the size, power, and cost of the sensor, which enables the deployment of small affordable GNSS-R satellites and their constellations.

GNSS-R technology has been demonstrated and can be used to retrieve various ocean and land parameters. Ocean altimetry is one of the most challenging applications of GNSS-R. The passive reflectometry and interferometry system (PARIS) for mesoscale altimetry was first proposed by Martín-Neira et al. [12]. In 1996, the first GNSS-R experiment for sea surface height estimations was conducted, and a root mean squared (RMS) height accuracy within 5 s of 1% of the used code chip (3 m for C/A code) was realized [13]. Since then, many studies have demonstrated spatial and/or temporal variation in sea levels using this new technique with an optimal accuracy of a few centimeters in ground-based or air-based experiments [14–18] and on the order of meters in space-borne missions [19]. Other organizations have conducted theoretical studies, the development of new receivers, and ground/air-based GNSS-R experiments and achieved encouraging results and progress.

Signal modernization and the development of the new generation of GNSS constellations, especially the successful construction of BDS [20], have allowed GNSS-R to use multi-frequency and multi-system signals freely. There are currently more than 120 GNSS satellites in orbit, which affords continuous, stable, and high-quality free L-band signals. More applications will be realized using these multi-frequency and multi-system GNSS signals as well as future space-borne GNSS-R missions. GNSS-R technology is expected to supplement sea level observations with high spatiotemporal resolution and high precision. This paper simply summarizes the current status of GNSS-R in sea level altimetry and our related work according to different kinds of data processing methods and equipment. The current development of multi-frequency and multi-system GNSS is also outlined. Furthermore, the future developments of receivers and space-borne GNSS-R missions are presented.

2. Current Status of GNSS-R Sea Level Altimetry

GNSS-R altimetry relies on the path delay or time delay between the reflected and direct signals to calculate the vertical distance between the antenna and the sea surface, i.e., reflector height, and then estimates sea level by subtracting the derived reflector height from the geodetic height of the antenna (see Figure 1). This technology can be roughly divided into two categories according to the equipment used. The first uses one GNSS

upward antenna to receive the direct and reflected signals simultaneously and is called GNSS interferometric reflectometry (GNSS-IR) or GNSS multipath reflectometry (GNSS-MR). The other kind of GNSS-R uses one upward and one or more downward antennas to separately receive the direct and reflected GNSS signals, and then these signals are further processed by a specially designed hardware or software-defined receiver to calculate the path delay. This kind of GNSS-R altimetry can be mainly divided into conventional GNSS-R (cGNSS-R) and interferometric GNSS-R (iGNSS-R) according to their different data processing methods. According to the different platforms for installing GNSS-R altimetric equipment, GNSS-R can be divided into ground-based (including ship-borne), air-borne, and space-borne GNSS-R. Meanwhile, GNSS-IR/MR can only be used for ground-based GNSS-R altimetry because weak multipath signals cannot be received by a high-altitude single-antenna platform. The following paragraphs will briefly introduce the principles and status of each kind of GNSS-R altimetry.

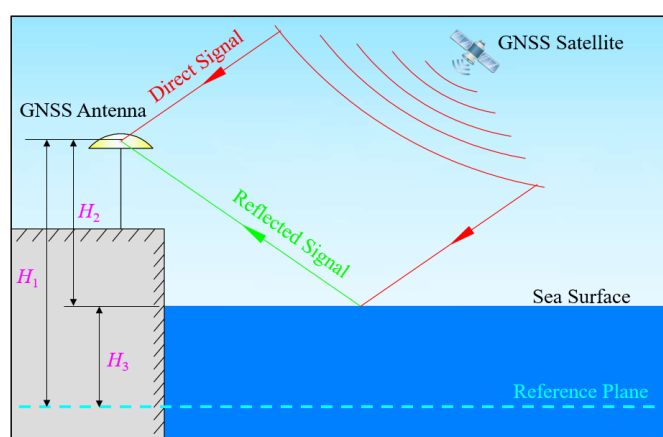


Figure 1. Schematic of the GNSS-IR experiment setup.

2.1. Sea Level Estimation Using GNSS-IR/MR

In traditional GNSS positioning, the upward geodetic antenna receives not only the direct signals from the GNSS satellite but also the reflected signals from the surroundings. This is called the multipath effect and should be eliminated to obtain a precise positioning result. However, Larson et al. [21] found that these multipath signals can also be used for GNSS-R; this is called GNSS-MR. Because the received direct and reflected signals interfere with each other and form a composite signal, this technology can also be called GNSS-IR. Sea level estimations based on this GNSS-R technique have been verified using data from existing global GNSS reference stations. Some studies have also focused on using low-cost receivers to estimate sea levels.

2.1.1. Geodetic Receiver

The geodetic receiver was first successfully used to measure coastal sea level 20 years ago [22]. Since then, the feasibility of using traditional geodetic GNSS instruments (receivers and antennas) to measure sea levels has also been demonstrated by many research groups worldwide. Basically, the method uses the signal-to-noise ratio (SNR) of GNSS observations to estimate sea level. The SNR is an index of the received signal quality, which is mainly affected by the antenna gain, receiver noise, and multipath effect. After being reflected from the sea surface, signals at a low elevation angle are still right-handed circularly polarized (RHCP), which can also be received simultaneously with the direct signal by the antenna. The composite signal oscillates with time because of the reflected signal. The GNSS SNR observation series is an interference signal composed of the direct and reflected signals as shown in Figure 2. The former is a low-frequency signal and can be obtained using

low-order polynomial fitting. After the direct signal is removed from the raw SNR series, the reflected (or multipath) signal can be obtained, and the signal can be expressed as [23]

$$SNR_m = A_m \cos(2\pi f(t) \sin \theta(t)) = A_m \cos(2\pi \frac{2H_2(t)}{\lambda} \sin \theta(t)), \quad (1)$$

where A_m is the amplitude of the reflected signal; λ is the wavelength of the GNSS signal; and $f(t)$, $H_2(t)$, and $\theta(t)$ are the signal frequency, reflector height, and satellite elevation angle at time t . Note that both the reflector height and the angle are time-related. Once the geodetic height of the antenna (H_1) is known, according to Figure 1, the sea level can be calculated via

$$H_3(t) = H_1 - H_2(t), \quad (2)$$

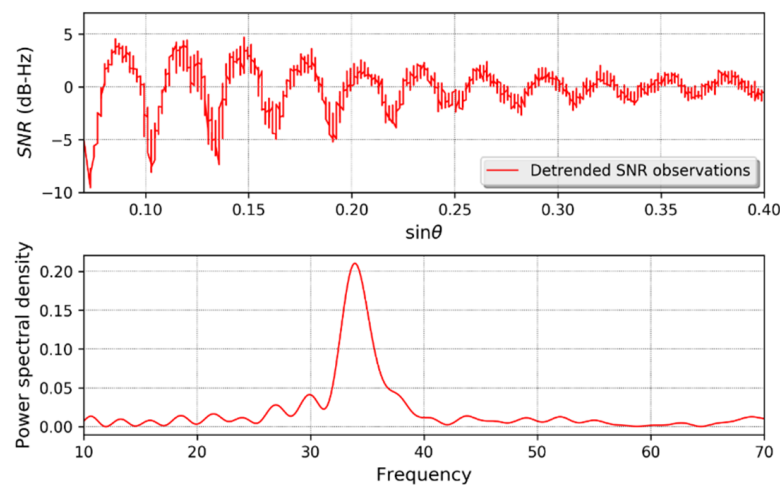


Figure 2. Upper: one example of the detrended SNR observations for BDS PRN 08 at B1 frequency at one station. **Below:** Lomb–Scargle periodogram (LSP) spectral analysis of the detrended SNR observations.

Because of the tidal effect, the reflector height changes significantly in most cases, which induces variation in the reflected signal frequency as in Equation (1). The amplitude of the reflected signal is also related to the GNSS antenna gain pattern, satellite elevation angle, and many other factors [24,25]. The amplitude decreases with increasing satellite elevation angle for a geodetic GNSS receiver collecting SNR observations. Thus, the reflected signal is a typical non-stationary signal and behaves like a damped sinusoid; that is, both the frequency and amplitude of the signal vary at different times. Estimating the frequency (or reflector height) from the non-stationary signal is the core of GNSS-IR-based sea level estimation. Sea level estimation using the existing geodetic receiver can be divided into two general types based on their different data processing strategies:

1. Spectrogram analysis: The frequency of the non-stationary signal is treated as a constant during a full satellite tracking period (e.g., 5° – 25°) [26]. Then, Lomb–Scargle spectral analysis is used to determine the peak frequency of the signal with a frequency resolution of 1 mm. One example of this method is shown in Figure 2. The temporal variation in the reflector height can be solved via height rate correction based on tidal harmonic estimation. Then, a piecewise cubic spline is used to fit the residuals. This method was proposed by [5,21]. In addition to Lomb–Scargle spectral analysis, wavelet analysis has been used to estimate the sea level [27,28]. Wavelet analysis performs better than the Lomb–Scargle method both in temporal and spatial resolution of the sea level. Wang et al. [29] also evaluated the performance of multi-frequency signals for different constellations, and a multi-GNSS combination algorithm was used to improve the accuracy of estimating the reflector height.

- SNR inverse modeling: Whereas spectrogram analysis uses an isolated period of SNR data to obtain a single measurement, this method is based on a forward/inverse approach to modeling the entirety of SNR observations [30,31]. The pre-fit residuals and parameter biases are calculated through a statistically rigorous inverse model, which is based on the physical forward model. The linear phase bias coefficient is related to the reflector height and thus the sea level. For each satellite track, an independent sea level estimation can be obtained. All the track-derived sea level estimations are combined to obtain a regularly spaced time series of sea levels based on a weighted moving average with a post-spacing of 1 h and a window width of 8 h [9,32]. Strandberg et al. [24] used a B-spline function to describe the temporal sea level (or the reflector height) variations to satisfy sea level continuity. The coefficients of the B-spline function can be determined through nonlinear Least Squares fitting of the SNR series. This method has significantly higher precision in sea level estimations than spectrogram methods (e.g., the FFT or Lomb–Scargle method). The method also contributes to a better spatial and temporal sampling of the sea surface. However, the method requires SNR observations in a full period (with the elevation angle basically from 5° to 25°), which induces significant time delays for GNSS-based sea level measurements. In [33], interval analysis was used to find the global optimization when using the model to fit the SNR data, and the proposed method improved both the precision and computation efficiency. Later, a sea level time series in the form of a B-spline curve combined with a Kalman filter was proposed to estimate sea levels in real time with high precision [25]. The method was successfully used to estimate sea level in real time with an RMS error of approximately 3 cm.

Non-SNR GNSS observations, including the code, phase, and signal strength indicator (SSI), suffer from the multipath effect. Therefore, when there are no SNR data for GNSS-IR altimetry, the code, phase, and SSI can be used instead for GNSS-IR sea level estimation. Reference [34] adopted a three-frequency code and phase combinations to estimate sea level with improved RMSEs of approximately 18 cm and 10 cm. To weaken the influence of main errors such as ionospheric and tropospheric errors, Wang et al. [35,36] proposed different combinations of dual-frequency codes and phases to estimate sea level. The detailed equations for these combinations can be found in Table 1. Figure 3 is one example of combined multipath errors and their corresponding Lomb–Scargle periodogram (LSP), from which two clear peaks can be discerned because dual-frequency signals were used. The results in these references verified the proposed methods, which provide substitutes for GNSS-IR technology and expand its applicability.

Table 1. GNSS-IR models and their corresponding formulas.

Model	Main Formulas *	References
SNR	$SNR = \frac{P_d + P_r + 2\sqrt{P_d}\sqrt{P_r} \cos(\psi + \varphi)}{P_{noise}}$	[35]
SSI	$SSI = \min\left(\max\left(\text{int}\left(\frac{P_d + P_r + 2\sqrt{P_d}\sqrt{P_r} \cos(\psi + \varphi)}{P_{noise}}\right), 1\right), 9\right)$	[37]
Combinations of code and phase	$M = \rho_1 - \rho_2$	[36]
	$N = \rho_1 - \rho_2 + L_1 - L_2$	[36]
	$N_{1,2,5} = \lambda_5^2(\rho_1 - \rho_2) + \lambda_2^2(\rho_5 - \rho_1) + \lambda_1^2(\rho_2 - \rho_5)L_4 = L_1 - L_2$	[34]
	$M_{1,2,5} = \lambda_5^2(L_1 - L_2) + \lambda_2^2(L_5 - L_1) + \lambda_1^2(L_2 - L_5)$	[35] [36]

* The definition of each variable in these equations is given in the corresponding references.

Because the sea surface is non-stationary during one-arc SNR observations, a dynamic sea level correction is usually adopted after a stationary reflector height, which is H_2 in Equation (1), obtained using spectrogram analysis on the SNR observations. Reference [21] showed that the stationary reflector height was biased by an amount equal to

$$\dot{H} \tan \theta / \dot{\theta}, \tag{3}$$

where $\dot{H}(= \frac{dH}{dt})$ defines the vertical velocity and $\dot{\theta}(= \frac{d\theta}{dt})$ defines the elevation angle velocity. The final sea level can be calculated using the following equation:

$$H_2 = \dot{H} \tan \theta / \dot{\theta} + H, \quad (4)$$

Reference [21] proposed a two-step iteration method: they first calculated the stationary reflector height H_2 using spectrogram analysis on the SNR observations without considering \dot{H} , and then estimated \dot{H} using this coarse $H_2(t)$ series to produce height corrections (Equation (3)). Finally, sea levels (H) can be calculated using Equation (4). Löfgren et al. [2] proposed a similar two-iteration method by calculating \dot{H} from daily sinusoidal functions fitted to the reflector heights $H_2(t)$ obtained from the first iteration. When using the method of SNR inverse modeling to estimate sea level, Roussel et al. [4] proposed a dynamic SNR method to substitute Equation (4) into Equation (1), and then combined all the satellites visible within each time window to conjointly estimate H and \dot{H} by a moving window and a classical Least Squares method. Wang et al. [29] expanded this dynamic SNR method to include the tropospheric delay correction, and found that multi-GNSS combination can improve the precision of the estimated sea level from GNSS-IR. Larson et al. [5] used quadratic B-splines functions to describe the dynamic sea levels, and Strandberg et al. [25] realized real-time sea level estimations with this dynamic sea level expression using Kalman filtering. Reference [38] used a cubic spline instead of Equation (4) to express the dynamic sea level, and estimated sea levels using a differential evolution method other than the Least Squares method. The experimental results showed that the proposed method led to a clear increase in precision compared to the results from the Least Squares method.

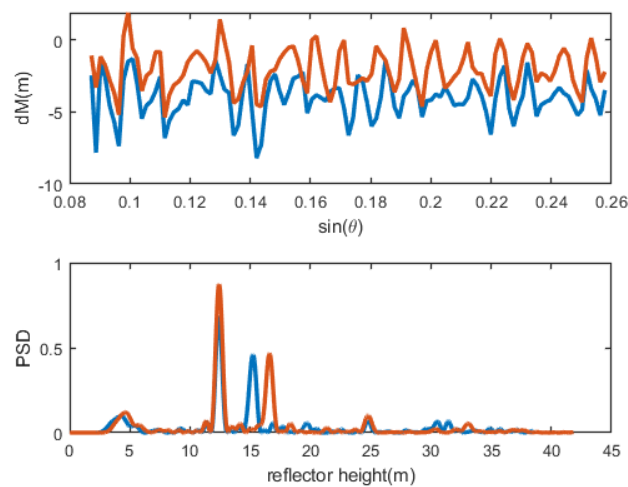


Figure 3. Example of two combined multipath errors (**top** panel) from a dual-frequency code combination for Galileo signals at station AT01 and their correspondent LSP figures (**bottom** panel), from which we can see two peaks corresponding to dual-frequency signals. The blue and red lines represent two different combined multipath errors.

2.1.2. GNSS-IR with a Low-Cost GNSS Receiver

In addition to the use of the geodetic receiver for GNSS-IR altimetry, a low-cost GNSS instrument has also been used to estimate the sea level in recent years. Li et al. [39] demonstrated the feasibility of estimating reflector height with consumer-grade GNSS chips and antennas. Williams et al. [40] showed that a low-cost GNSS instrument can also estimate sea level well with an RMS error of approximately 5 cm. An Android-based tablet or phone collecting SNR observations can also be used to monitor sea levels [41,42]. In a Huawei P30 phone experiment, the BDS B1I, GPS L1, and GLONASS G1 provided more precise and stable height retrievals than those from GPS L5 and Galileo E5a. Fagundes et al. [43] demonstrated an open-source platform integrated with an Arduino system and a

low-cost GNSS module. The platform-based sea level estimations agree well with the in situ ones with an RMS error of approximately 3 cm. Overall, a low-cost GNSS receiver can be used to estimate sea level with lower cost and better data availability than conventional geodetic receivers, and it provides a promising method for future GNSS-IR applications.

2.2. GNSS-R Altimetry with Two or More Antennas

Sea level estimation based on GNSS-R relies on the accurate acquisition of the delay between the reflected and direct signals. Figure 4 shows the schematic of ground-based and air-borne GNSS-R altimetry with two antennas. For GNSS-R setups with two or more antennas, one upward antenna is used to receive the direct GNSS signals, and one or more downward antennas are used to receive the reflected GNSS signals from the sea surface. The two signals are further processed using a specially designed hardware or software-defined receiver to calculate the path delay between the reflected and direct signals. Because of the different path delay acquisition methods, different signal processing methods for the receiver have been developed to calculate the delay, including conventional GNSS-R (cGNSS-R), interferometric GNSS-R (iGNSS-R), reconstructed-code GNSS-R (rGNSS-R), and partial interferometric GNSS-R [44].

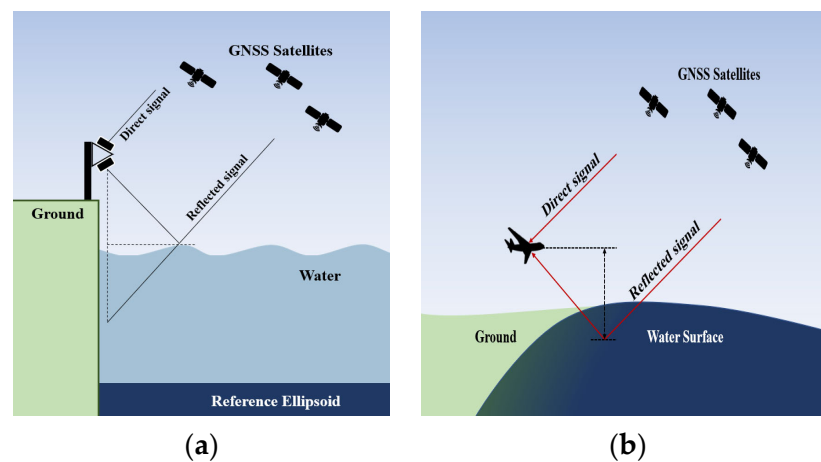


Figure 4. Schematic of (a) ground-based and (b) air-borne GNSS-R altimetry with two antennas.

2.2.1. cGNSS-R Altimetry

cGNSS-R acquires the path delay by correlating the reflected signal with a locally generated clean replica of the transmitted signal using the information of the direct signal [44], with the following correlation power [45]:

$$Y^c(t, \tau, f_d) = \frac{1}{T_c} \int_t^{t+T_c} s_R(t') a^*(t' - \tau) e^{-j2\pi(F_c + f_d)t'} dt', \quad (5)$$

where t is the integration start time; T_c is the coherent time, which is typically 1 ms; $s_R(t')$ is the reflected signal; $a^*(t' - \tau)$ is the local replica of the transmitted signal; τ is the time delay between the reflected and transmitted signals; and F_c and f_d are the central frequency and Doppler frequency shift. To improve the SNR, incoherent integration is required to obtain a 2-D delay-Doppler waveform (DDM) as

$$\langle |Y^c(\tau, f_d)|^2 \rangle \approx \frac{1}{N_i} \sum_{n=1}^{N_i} |Y^c(t_n, \tau, f_d)|^2, \quad (6)$$

where N_i is the number of incoherent averages. Figure 5 shows examples of measured 2-D delay-Doppler waveforms and their corresponding 1-D delay waveforms for a ground-based and a space-borne GNSS-R experiment. The path delay between the reflected and direct signals can be calculated using waveform retracking according to the 1-D delay waveforms. Four different retracers, namely the peak value of the 1-D delay waveform,

DER (the maximum of the 1-D delay waveform's first derivative), HALF (a fraction of the peak power in the 1-D delay waveform), and FIT (the fitting of the 1-D delay waveform to its model), are usually adopted to determine the time delay.

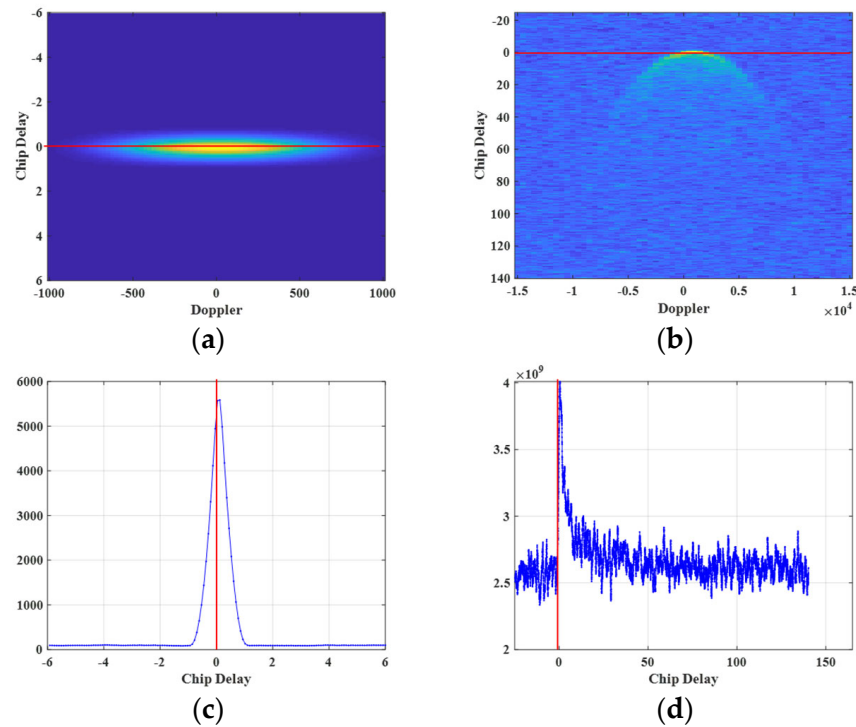


Figure 5. Measured 2-D delay-Doppler maps (a,b) and 1-D delay maps (c,d) for a ground-based (a,c) and a space-borne (b,d) GNSS-R experiment.

Then, for ground-based or air-borne GNSS-R altimetry, in which the curvature of Earth can be ignored, the reflector height can be deduced using the following equation according to the GNSS-R geometry as shown in Figures 4 and 6a:

$$\Delta H = -\frac{\delta\rho - (\delta\rho_{iono} + \delta\rho_{tropo} + \delta\rho_{rough} + \delta\rho_{ins})}{2 \cos \theta}, \quad (7)$$

where ΔH is the vertical height between the phase center of the reflected antenna and the sea surface, $\delta\rho$ is the observed path delay, $\delta\rho_{iono}$ and $\delta\rho_{tropo}$ are the ionospheric and tropospheric delay errors, $\delta\rho_{rough}$ is the error caused by the sea roughness, and $\delta\rho_{ins}$ is the instrumental error.

However, in space-borne GNSS-R altimetry, the curvature of Earth cannot be ignored, and the reflector height can be deduced as shown in Figure 6b using the following equation [46]:

$$\Delta H = \frac{\delta\rho - (\delta\rho_{iono} + \delta\rho_{tropo} + \delta\rho_{rough} + \delta\rho_{ins})}{2 \sin \theta} + r_s - r_E, \quad (8)$$

Where r_E is the Earth's spherical radius, r_s is the distance between the specular point and the geocenter, and γ is called the direction angle of the specular reflection point as shown in Figure 6b.

Then, the sea surface height can be calculated by subtracting ΔH from the geodetic height of the reflected antenna using Equation (2).

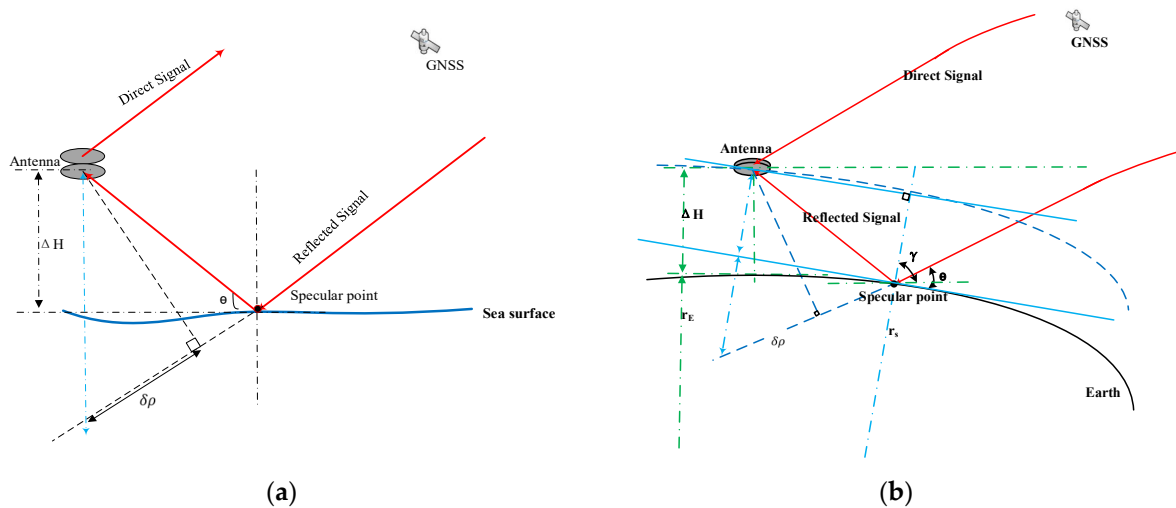


Figure 6. Geometry of GNSS-R altimetry when (a) considering the Earth as a flat surface, and (b) considering the Earth's curvature.

Small antennas are enough for cGNSS-R to receive multiple reflected GNSS signals, and therefore can be used for all kinds of platforms such as ground-based, air-borne, and space-borne platforms. Moreover, because of their low cost, several space-borne GNSS-R satellites can make constellations to improve the spatiotemporal resolution and revisit period of the observations. Because the very narrow bandwidth of GNSS signals limits the altimetric performance of cGNSS-R, rGNSS-R was also proposed to overcome the bandwidth limitation. The method of rGNSS-R is similar to that of cGNSS-R but uses a semi-codeless technique to reconstruct the wideband encrypted P(Y) or other codes before they are correlated with the reflected signal as described in [47,48]. However, most of the current space-borne GNSS-R missions use the cGNSS-R method because it is easy to realize practically. Therefore, cGNSS-R is widely used for remote sensing applications.

- (1) Ground/ship-based GNSS-R: Ground-based GNSS-R altimetry can be an effective supplement to existing TG stations and radar altimetry for sea level monitoring in coastal areas. Ground/ship-based GNSS-R altimetry includes code-based and phase-based methods according to the observables. The experimental configuration usually contains two antennas: one upward RHCP antenna to receive the direct GNSS signal and a downward left-handed circularly polarized (LHCP) antenna to receive the reflected signals from the sea surface. Then, the two signals are processed using a dedicated software-defined or hardware receiver to obtain the code delay or phase delay between the two signals. The accuracy of sea level measurement for code-based GNSS-R is limited to the meter or decimeter level because of the code chip length of GNSS signals. Centimeter-level sea levels can be determined using phase-based GNSS-R when the sea surface is relatively calm. However, when the sea becomes rough, the phase cannot be continuously tracked, and this method may fail.

The following are some examples of ground/ship-based cGNSS-R altimetry. In 2001, Treuhaft et al. [49] made estimates of lake surface height with a 2 cm precision in 1 s using reflected GPS signals observed from a 480 m Cloudcap Lookout point. In 2015, two BeiDou-R coastal experiments including lake and ocean experiments were performed in China [50]. The lake experiment had resulting errors of 0.11 m for geostationary Earth orbit (GEO) satellites and 1.61 m for inclined geosynchronous orbit (IGSO) satellites. In addition, the precision of the retrieved ocean height reached 0.37 m. In 2018, a shipborne GNSS-R code-level experiment based on GPS and BDS signals was conducted and realized sub-meter-level accuracy [51]. A coastal experiment using BDS-3 B1C and B2a signals showed that GNSS-R code-level altimetry could achieve centimeter-level precision through the application of the moving average [52].

In 2020, Wu et al. [53] verified the capability of code-based altimetry using reflected signals from BDS GEO satellites with decimeter-level precision.

- (2) **Air-borne GNSS-R altimetry:** For ground-based GNSS-R altimetry, the observation area is limited to only 1 km around the station, whereas air-borne GNSS-R altimetry can cover bigger observation areas. In 2002, Lowe et al. [14] presented the first two aircraft GNSS-R ocean altimetry measurements. The first experiment demonstrated 14 cm precision single-satellite altimetric measurements [54], and the second used authorized P(Y) codes to demonstrate 5 cm altimetric precision with 5 km spatial resolution [14]. In 2004, Ruffini et al. [15] used two synchronous GPS receivers flown at a 1 km altitude to collect L1 reflections from the sea surface to assess the altimetric precision and accuracy. The 20 km averaged GNSS-R absolute altimetric solution with respect to the Jason-1 sea surface height (SSH) and a GPS buoy measurement had an RMS error of 10 cm with a 2 cm mean difference. In 2014, sea surface topography in the Mediterranean Sea near Italy was deduced from an air-borne GNSS-R experiment using carrier phase data. The results revealed that eight tracks with centimeter precision were obtained between 11° and 33° of elevation, while at higher elevation angles, the number of tracks was significantly reduced owing to surface roughness [55]. In 2016, an air-borne GNSS-R altimetric experiment was conducted in Monterey Bay, California, and sea levels were observed with a standard deviation of 0.6 m using GPS L1 P-code data [56]. Air-borne GNSS-R altimetry has already proven its feasibility, and it has better flexibility and can cover a big observation area. However, it is not usually adopted because of the expensive fuel consumption of an airplane.
- (3) **Space-borne GNSS-R altimetry:** Space-borne GNSS-R satellites are equipped with small GNSS-R payloads to collect GNSS signals reflected off the sea surface, generating delay-Doppler maps (DDMs) or carrier phase measurements, which are then used to obtain the SSH. Space-borne GNSS-R can be regarded as a bistatic passive radar that processes the forward scattering signals (as shown in Figure 7). Compared with other space systems, space-borne GNSS-R has many characteristics: the system does not transmit any signals, thereby reducing the hardware requirements; with hundreds of GNSS satellites as illumination opportunities, more observations can be obtained with one track; the system can work in all weather conditions [42,57,58].

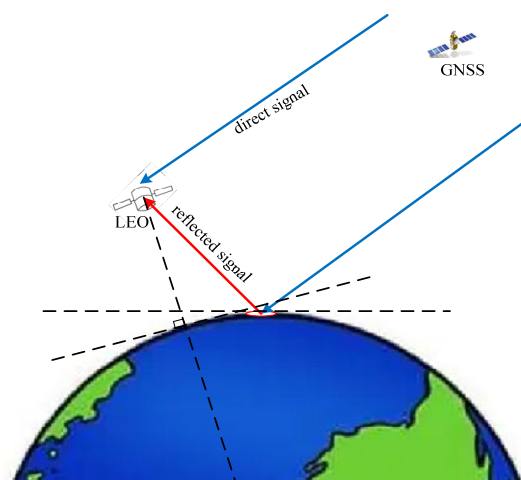


Figure 7. Schematic of space-borne GNSS-R altimetry with two antennas in which the Earth's curvature should be considered.

Space-borne GNSS-R has a high spatial and temporal resolution, which is very important for geodesy, geophysics, oceanography, and environmental research [59–61]. With C/A code signals, the size of the first Fresnel zone can be dozens of kilometers. However, the resolution can be further improved with proper antenna hardware and satellite orbit design [62,63]. In 2011, Gleason et al. [64] analyzed the fading statistics and sensing accuracy

of ocean-scattered GNSS and altimetry signals detected in a low Earth orbit (LEO). In 2016, the Cyclone American Global Navigation Satellite System (CYGNSS) was launched, aiming to monitor the sea surface wind. Its spatial resolution is 25 km, and its mean revisit time is 7.2 h. Despite C/A codes, there are many different signals broadcasting to the public. Cramér–Rao bound (CRB) analysis is used to obtain accurate altimetry with L1, E1, L5, E5, and E6 signals. E5 has the best altimetry performance when PARIS is used with the largest bandwidth [65]. In 2016, the first space-borne observation of sea surface height was conducted through GPS reflectometry with meter-level precision using the TechDemoSat-1 platform [66]. In addition, the multi-looking method based on the SAR principle can extract more observations in one track [67].

Owing to the advantages of GNSS-R, many GNSS-R space-borne missions have already been launched or will be launched in the future. The most famous and publicly available missions are TDS-1 and CYGNSS [6,67]. Most public research is based on the DDM or raw data of these two missions. The 3Cat-2 program uses semi-codeless technology to process P(Y) codes and achieve high-precision altimetry [68]. In 2011, the European Space Agency (ESA) proposed the PARIS in-orbit experiment using the iGNSS-R method [69]. In 2016, the ESA discussed a GEROS-ISS mission to determine sea surface height and wind speed [70]. In 2021, Unwin et al. [71] described the concept, case studies, and new technologies of HydroGNSS. In 2023, Chen et al. [72] retrieved ocean wind speeds for the BF-1 Mission. Additionally, Wang et al. [73] obtained and assessed wind speed products using the Jilin 1 Kuanfu 01B satellites. Though HydroGNSS, BF-1 and Jilin 1 are not designed for altimetry at first, they provide more opportunities for altimetry.

Space-borne GNSS-R involves taking measurements of two observables, the group delay and phase delay, which can be used to calculate the sea surface height according to the altimetry model. The group delay can be extracted from the reflected waveform, which can be obtained in most cases. The reflected waveform must be retracked to improve the accuracy. The three retrackers often used are DER, HALF, and FIT. In 2016, Mashburn et al. [56] used several methods to extract the group delay in an air-borne experiment. They extracted the global sea surface height with a mean height residual of 6.4 m compared with the mean sea surface (MSS) using TDS-1 data [74]. In 2017, Rius et al. [75] studied the ice sheet altimetry in Greenland with TDS-1 data, and the results showed good consistency with the ICESat sensor. In 2017 and 2020, Cartwright et al. constructed the first digital elevation model (DEM) based on TDS-1 data, demonstrating the application potential of space-borne GNSS-R in polar and glacial areas [76,77]. In 2020, Li et al. [78] evaluated altimetry performance using raw data from CYGNSS, with ranging accuracy reaching 3.9 and 2.5 m for the 1 s GPS and Galileo group measurements [79]. The results using the BDS-3 signals show the same accuracy as those using the other GNSS signals and are presented later [80]. In 2021, Zhang et al. [81] discussed error models for the TDS-1 data and improved the accuracy of group delay altimetry.

Phase-delay measurements have better accuracy than group-delay measurements. However, most GNSS-R observations involve diffuse scattering, which causes a phase shift and jumps randomly. However, the phase delay can be recovered and high-precision altimetry can be achieved in some cases. In 2004, Cardellach et al. [82] first extracted the interference phase of the reflected signals from an ice surface in the CHAMP satellite mission. The vertical accuracy was 0.7 m for 1 km sampling compared with that of the digital elevation model (DEM). In 2016, Semmling et al. [83] discussed several issues related to space-borne GNSS-R phase altimetry, proving that carrier phase observations are more sensitive to the terrain. In 2017, Li et al. [78] processed the TDS-1 signals from sea surfaces at high elevation angles. Compared with the MSS, the root mean square was 4.7 cm. In 2018, CYGNSS signals reflected off a lake were further studied. The phase-delay altimetry performed much better than that of the group delay [84]. Under grazing angle geometries, the maximized coherent scattering enables the carrier phase-delay altimetric technique over the sea, which can provide precise ranging measurements. In 2020, Cardellach et al. [19] proposed the use of grazing angle geometry to achieve precise phase-delay altimetry

from CYGNSS data. The altimetric precision reached 3/4.1 cm (median/mean) at 20 Hz sampling, and cm level at 1 Hz, which is comparable to that achieved by radar altimeters at 1 Hz sampling. Moreover, they found that the requirements for wind and waves to enable coherent scattering at grazing angle geometries were below 6 m/s wind and 1.5 m significant wave height. In 2021 and 2022, an improved method for extracting coherent components from signals was proposed by Wang et al. [85,86], who processed CYGNSS data to measure sea surface elevation and a river gradient with high precision. In 2020 and 2022, Nguyen and Roesler used Spire constellation data to show that most coherent events occur in areas covered by sea ice, and their carrier phase height measurement reached an accuracy on the centimeter level [87,88].

Owing to the significant difference in space paths between the direct and reflected signals in space-borne GNSS-R, there are many error sources that must be carefully considered. LEO satellites have a real-time orbit determination accuracy approximately at the meter level, which does not meet the requirement for precise altimetry. The various error sources that need to be modeled include time tag synchronization, ionospheric and tropospheric delays, baseline offset between the positioning antenna and the downward antenna, ocean and solid earth tides, and other sources. At present, public space-borne GNSS-R data are mainly at the L1 frequency, and the accuracy is at the level of several meters. Although phase-delay altimetry is as precise as traditional satellite altimetry, the required conditions are relatively strict, mainly occurring in situations such as low elevation in calm sea or ice.

The details of some typical references for GNSS-R altimetry are listed in Table 2. To sum up, carrier phase altimetry can realize more precise altimetric results than code-delay altimetry, and centimeter-level altimetric results can be expected to be realized in the future. However, there are still some unresolved issues that make achieving this goal a great challenge.

Table 2. Details of some typical references for GNSS-R altimetry.

Reference	Platform	Signal	Reflection Surface	Precision
Treuhaft et al., 2001 [49]	From a 480 m Cloudcap Lookout point	GPS code	lake	2 cm
Zhang et al., 2015 [50]	Ground-based	BDS code	lake; ocean	0.11 m for GEO and 1.61 m for IGSO; 0.37 m
Gao et al., 2018 [51]	Ship-borne	GPS and BDS code	ocean	Sub-meter-level
Gao et al., 2021 [52]	Ground-based	BDS-3 B1C and B2a	ocean	Centimeter-level after using moving average
Wu et al., 2020 [53]	Ground-based	BDS GEO code	ocean	Decimeter-level
Lowe et al., 2002 [14]	Air-borne	GPS C/A and P(Y)	ocean	14 cm for C/A and 5 cm for P(Y)
Ruffini et al., 2004 [15]	Air-borne	GPS L1	ocean	10 cm
Semmling et al., 2014 [55]	Air-borne	GPS carrier phase	ocean	8 of 65 tracks with centimeter precision
Mashburn et al., 2016 [56]	Air-borne	GPS L1 P-code	ocean	Std: 0.6 m
Clarizia et al., 2016 [66]	Space-borne: TDS-1	GPS group delay	ocean	Meter-level
Mashburn et al., 2016 [74]	Space-borne: TDS-1	GPS L1 C/A	ocean	A mean height residual of 6.4 m
Li et al., 2020 [78]	Space-borne: CYGNSS	GPS and Galileo group delay	ocean	3.9 and 2.5 m for the 1 s GPS and Galileo group measurements
Zhang et al., 2021 [81]	Space-borne: TDS-1	group delay	ocean	
Cardellach et al., 2004 [82]	CHAMP satellite mission	phase delay	sea ice	0.7 m for 1 km sampling
Li et al., 2017 [78]	Space-borne: TDS-1	phase delay	sea surface	RMS: 4.7 cm RMS: 0.68 m
Li et al., 2018 [84]	Space-borne: CYGNSS	group delay; carrier phase delay	lake	The difference between the derived results and the geoid model is ~15–20 cm
Cardellach et al., 2020 [19]	Space-borne: CYGNSS	grazing angle phase delay	ocean	3/4.1 cm (median/mean) at 20 Hz sampling
Nguyen and Roesler, 2022 [88]	Space-borne: Spire constellation	carrier phase	sea ice	Centimeter level

- (4) GNSS-R dedicated receiver: The receiver is a core component that has a significant impact on GNSS-R sea surface height measurements. It needs to be different from

the geodetic receiver because it needs to provide path delays between the direct and reflected signals, and the accuracy of the estimated path delays greatly determines the accuracy of the final altimetry results. In addition, algorithms need to be integrated into the baseband signal processing of the receiver for situations in which the reflected signals are generally weakened and scattered by the sea surface. Therefore, the development of the recorder, to some extent, affects the GNSS-R measurement accuracy.

There are two main types of GNSS-R receivers: the hardware receiver and software-defined receiver (SDR). The hardware receiver can efficiently process satellite signals and is widely used because intensive cross-correlation computation is required for GNSS-R. Meanwhile, the SDR has been and will continue to be a valuable research tool given its flexibility and easy modification for different GNSS signals. In the early stage, a receiver named GOLD-RTR was developed for cGNSS-R, and it can process L1 band signals to output DDM measurements [89]. Afterward, IEEC-ICE produced an aircraft version of the PARIS Interferometric Receiver (PIRA) for iGNSS-R. This system can also process GPS L1 C/A signals [90]. Another receiver named GORS was designed to output interference phase information, which can support GPS L1/L2 and Galileo E1 band signals [91]. The receiver of the first Chinese GNSS-R satellite mission BuFeng-1 can process GPS L1/BDS B1 reflected signals into DDMs, and it has been applied to soil moisture and wind speed retrieval [92,93]. A receiver named GNOS II has been designed for the FY-3E satellite and can provide DDMs to monitor sea waves and ocean wind [94,95]. However, owing to the development of GNSS-R, its algorithms are rapidly iterative, which leads to the extensive use of SDRs for convenient code modification. The microwave interferometric reflectometer is a multi-beam dual-band (L1 and L5) instrument built to assess the performance of the PARIS-IoD mission [96]. The Flexible Microwave Payload is a remote sensing payload based on a software-defined radio and is integrated with GNSS-R and a total power radiometer [97].

Several teams have developed GNSS-R SDRs for monitoring ocean and soil moisture. An altimetry SDR was proposed by the Jet Propulsion Laboratory in the early years. This is capable of processing GPS C/A code and P(Y) code to export DDMs and interference phase information [7]. Shortly afterward, OCEANPAL was developed by Starlab. It delivers Level-2 data, the sea surface height and the significant wave height, for operational coastal monitoring [98]. Around the same time, a GPS-based SDR was developed by the Beijing University of Aeronautics and Astronautics (China) to monitor sea surface wind and soil moisture [99]. In 2014, a GLONASS-based SDR was also developed that can obtain better solutions than GPS-based SDR [100]. PYCARO is focused on ground-based, air-borne, and space-borne altimetry applications and can track both C/A and P(Y) GPS signals [48]. On the basis of the PARIS concept proposed by the European Space Agency for GNSS-R altimetry, an interferometric SDR was designed to process broadband signals including L1, L2, and L5 [101]. In 2017, CNES proposed an open-source SDR that can perform carrier phase altimetry. It allows extending the coherent integration time well beyond the limit of a C/A code message bit length on the reflected signals [102].

A field programmable gate array (FPGA) is another alternative. This method combines the advantages of the hardware receiver and the SDR, and it meets the requirements of efficiency and flexibility. In 2017, an instrument based on an FPGA for CubeSats was designed and implemented to extract sea ice and soil moisture [103]. More recently, an FPGA-based GNSS-R receiver was developed that can detect and track direct and reflected GPS L1 C/A signals and generate high-resolution and real-time DDMs [104]. However, it needs an expensive FPGA to provide enough power for parallel computation. A more cost-effective option is using a graphics processing unit (GPU) to improve SDR efficiency. Several works have proven the efficiency of GPUs in GNSS-R receivers. It should be noted that mobile phones can also be receivers to sense water and soil via GNSS-IR [41,105,106].

2.2.2. iGNSS-R Altimetry

iGNSS-R is different from cGNSS-R in that it acquires the path delay by correlating the reflected signal with the direct signal instead of the replica. Therefore, iGNSS-R does not

need to know the structure of the ranging code and can extract all the spectral components of the GNSS signals. In 1993, Martin-Neira [12] first proposed the concept of PARIS based on iGNSS-R for ocean altimetry. This method does not need knowledge of the structure of the ranging code and directly correlates the reflected signal with the direct one to obtain the delay. Compared with cGNSS-R, it exploits the full bandwidth of the transmitted GNSS signal without knowledge of the actual ranging codes to improve the ranging performance for ocean altimetry [78]. In 2012, Rius et al. [18] conducted the first proof-of-concept experiment to demonstrate the feasibility of iGNSS-R for ocean altimetry from a bridge, and achieved a 7.5 cm uncertainty in 1 s measurements [18]. To verify the feasibility of this concept for ocean altimetry, a shore-based experiment using the GPS L1C/A signal was performed in 1997 in Rotterdam (the Netherlands) [13]. The altimetric accuracy was approximately 3.3 m, which was approximately 1% of the L1C/A code chip length. Several iGNSS-R designs for ocean applications have also been proposed, such as Paris-IoD [107], GEROS-ISS [70], G-TERN [108], and “Cookie” [109]. In 2010, Rius et al. [110] first formalized the retracking of GNSS reflections using the derivative of their waveforms, and applied PARIS to estimate SSH from one flight experiment in the North Sea off the coast of Norway. The iGNSS-R waveform tracking and retracking procedure for a space-borne mission is illustrated in [111,112]. In 2014, Cardellach et al. [113] conducted an air-borne experiment at a 3 km altitude to consolidate the precision of iGNSS-R ocean altimetry and realized a precision of 22 cm in 65 km along-track averaging. The results also verified that iGNSS-R is at least two times more precise for sea surface altimetry than cGNSS-R. In 2014, Pascual et al. [65] analyzed the precision bounds of iGNSS-R for GPS L1 and L5 signals and Galileo E1, E5, and E6 signals, and the results showed that the precision was less than 20 cm. In 2019, Fabra et al. [114] analyzed multiple and simultaneous reflected air-borne GNSS signals at two frequency bands (L1 and L5) to realize iGNSS-R ocean altimetry. This included signals from two GPS and two Galileo satellites. The obtained results agreed well with ancillary information at the 0.40 m level.

In 2014, Li et al. [115] presented a new on-board processing method based on iGNSS-R called partial interferometric GNSS-R, which uses the interferometry of partial GNSS signal components to further improve altimetry precision. Then, in 2016, they found that neglecting the inter-modulation component of the GNSS signals would result in underestimating the final iGNSS-R altimetric precision by a factor of 1.5–1.7 [78].

iGNSS-R has less complex tracking and retracking strategies and higher final altimetric precision than cGNSS-R. However, because the wideband signal brings high thermal noise in iGNSS-R, high-gain and high-directivity antennas are required. Moreover, owing to the cross-correlation between the reflected and direct signals, iGNSS-R cannot distinguish GNSS satellites according to the code structure. Simultaneously tracking multiple GNSS signals in a space-borne iGNSS-R mission requires a high-gain digital multi-beam phased array antenna, which makes the iGNSS-R system more complex and expensive than a cGNSS-R system.

2.3. Multi-Mode and Multi-Frequency GNSS-R Altimetry at Our University

Since 2017, we have conducted some research mainly on GNSS-IR and ground/ship-based cGNSS-R altimetry, including theory, algorithms, and instrumentation, and the following are brief descriptions of this work.

2.3.1. GNSS-IR Altimetry

Considering the possible absence of SNR in conventional GNSS observation files, on which GNSS-IR relies, different alternatives for SNR observables in GNSS-IR were found and tested for estimating sea levels. Two combinations of code and carrier phase were proposed to realize GNSS-IR sea level estimation [36]. GPS, Galileo, GLONASS, and BDS triple-frequency signals were used to compose different combinations to estimate the sea level. The experimental results show that the two combination methods can estimate sea levels with a precision of 15–19 cm, which is similar to that of the traditional SNR

method for station AT01 in Alaska. The proposed methods provide alternatives for sea level estimation using GNSS-R technology. In 2018, non-geometric linear combinations of carrier phases for sea level altimetry were presented for the first time on the basis of dual-frequency GNSS signals [35]. Different types of GNSS observation and retrieval methods were tested in the data processing. The experimental results showed that sea levels determined from GPS SNR and the proposed method agreed well with a correlation coefficient of 0.97–0.98 and RMSE values less than 0.2 m for station SC02 in the US. We also proposed using SSI data in GNSS observation files for estimating sea levels, which is an alternative to existing methods because SSI data always exist [37]. Four multi-GNSS and multi-frequency datasets from three stations (SC02 in the US, station AT01 in Alaska, and station HKQT in Hong Kong) were used to monitor sea level. Sea level estimations with RMSEs of 7–8, 5–9, 12–15, and 9–13 cm relative to in situ data were realized for these four datasets using the proposed method, and the correlation coefficients for these stations were bigger than 0.98, 0.98, 0.93, and 0.96, respectively, which are similar to those of the traditional SNR method. We conducted further tide analysis on sea level results retrieved from the proposed method, and the ocean tide coefficients for several main tides determined from different data agreed well. These proposed methods are illustrated using equations in Table 1. The definition of each variable in these equations is given in the corresponding references.

2.3.2. GNSS-R Altimetry with Two Antennas

For cGNSS-R, we have designed a GNSS-R SDR based on Matlab for sea surface altimetry and soil moisture monitoring. This SDR can process L1, L2, L5, B1, and B2 band signals, and several ship-borne [51], coastal [52,116,117], and land-borne [118] experiments have verified its satisfactory performance. Because of a lot of cross-correlation in GNSS-R data processing, this SDR can only perform post-processing. A GPU and a conventional central processing unit (CPU) were used simultaneously (see Figure 8) to realize the design of a real-time GNSS-R SDR for coastal altimetry [119]. Complex cross-correlation is handled by the GPU, while simple computations are handled by the CPU to improve the computational efficiency. A 12 h coastal GNSS-R experiment verified the capability of the real-time SDR. After a 15 min moving average filter is used on the initial altimetric results, the RMSE of sea levels derived from the Quasi-Zenith Satellite System (QZSS) GEO is approximately 8.36 cm, which outperforms other signals. Meanwhile, among the other IGSO or medium-Earth-orbit (MEO) satellites, the RMSE of the sea levels derived from BDS (13.56 cm) is better than those from QZSS (21.26 cm) and GPS signals (22.42 cm).

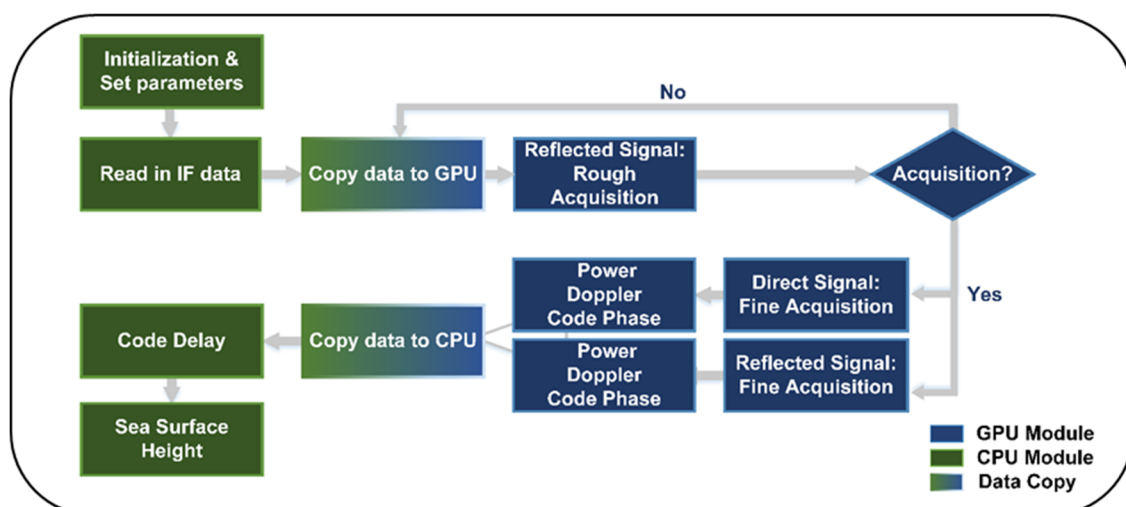


Figure 8. Flowchart of the real-time GNSS-R SDR. Modules with different single colors are handled by the GPU and CPU. The mixed-color modules represent data transfer between the CPU and the GPU as depicted in [119].

Different kinds of GNSS-R experiments have also been conducted in the past several years. Using the coastal experimental data, we first evaluated the code-delay altimetry performance of the BDS-3 system with the new broadcasting signals of B1C and B2a. With a 5 min moving filter, the RMSE is 5.3 cm for B1C and 11.1 cm for B2a as shown in Figure 9 [52]. In GNSS-R code-delay altimetry, when the path delay between the direct and reflected signals is less than one chip length, the delay waveform of the reflected signals is distorted and results in decreasing precision of the derived sea levels. This is because of crosstalk, which means the direct signal leaks into the downward antenna. He et al. [120] used the L5 signals from the QZSS to analyze the crosstalk between the direct and reflected signals. Then, an EMD filter and waveform correction were used to weaken the crosstalk, and the RMSE improved to 9.5 cm for L5 signals. The delay map of the crosstalk signals is shown in Figure 10. The power waveform of the reflected signals, the crosstalk signals, and the synthetic signals at one epoch are shown in this figure. It is shown that the code-delay observations are biased because of the delay error caused by the crosstalk, which will finally decrease the altimetric precision. In addition, the bias cannot be mitigated by the non-coherent averaging method given the approximately constant value.

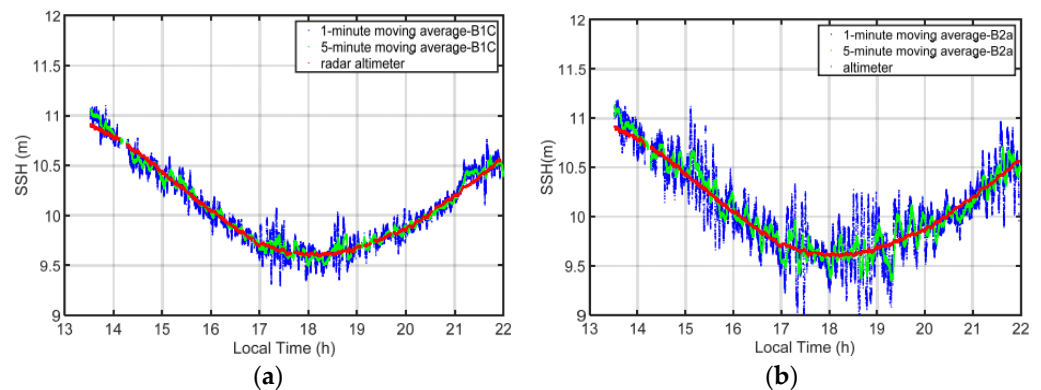


Figure 9. Sea surface heights derived from (a) B1C and (b) B2a code-level measurements with the moving average and radar altimeter data in one coastal GNSS-R experiment as reported in [52].

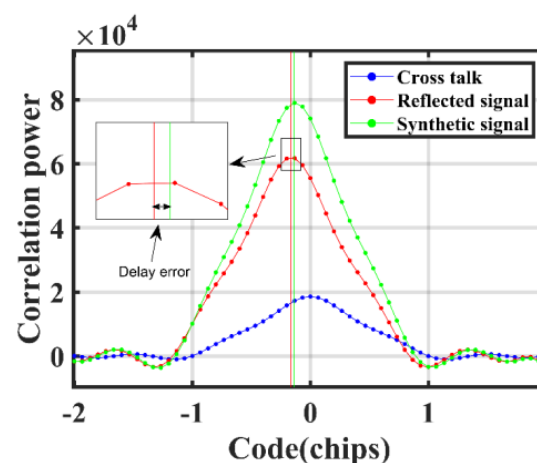


Figure 10. Delay map of the crosstalk signal in one coastal GNSS-R experiment as reported in [120].

With the full construction of QZSS and BDS-3, GNSS can provide more precise code observations owing to their advanced signal modulation. We tested interoperable signals with a frequency of 1575.42 MHz, i.e., L1C/A and L1C from QZSS and B1C from BDS, for GNSS-R altimetry simultaneously, and proposed a joint weighted GNSS-R altimetry method to improve sea level precision using combinations of multi-signals. The experimental results showed that the performance of GNSS-R altimetry based on binary offset carrier modulation signals was better than that of binary phase shift keying.

Moreover, the proposed joint weighted GNSS-R altimetry method further improves altimetry precision [117]. Considering the optimal accuracy of shore-based GNSS-R code-delay sea level measurements is only at the decimeter level, Ning et al. [121] proposed using Fourier series fitting to optimize the GNSS-R code-delay altimetry results. The RMSEs of three GNSS-R altimetric data were improved from 70–90 cm to 9–15 cm. The results indicate that the proposed method not only optimizes the GNSS-R code-delay height measurements and supplements the missing data, but also predicts future sea levels with high precision.

An in-harbor and off-shore experiment on ship-borne GNSS-R code-delay altimetry was conducted in which the equipment was set up on a Chinese research/survey vessel, Xiang Yang Hong 06. Figure 11 shows the estimated reflector heights based on GPS and BDS signals with different cut-off elevation angles for the in-harbor and off-shore shipborne experiments, respectively. The moving average values with a 10 min window are drawn in green. Different cut-off angles of satellites are considered for both experiments. For in-harbor experiments, the mean values of derived reflector heights are within 10 cm for both a 50° cut-off angle and a 30° cut-off angle, while for STD values, a 50° cut-off angle performs better, while for the off-shore experiment, the STD of BDS-R-derived results show a different performance. In general, as shown in Figure 11, the mean values and standard deviations (STDs) of the derived reflector heights show good consistency with the BDS B1I and L1C/A signals. Moreover, the results retrieved from BDS-3 and GPS satellites are more precise than those from BDS-2 satellites [52].

The precision of the initial code-delay altimetry was optimal at the decimeter level because of the width limitation of the code chip. Because the phase of the GNSS signal can afford more precise distance observation, we also conducted GNSS-R phase-delay altimetry. Using the L1 signals from the QZSS GEO satellites improves the phase altimetry performance, and the accuracy is 1.4 cm [122]. However, when the sea becomes rough, the phase cannot be continuously tracked, and the phase altimetry fails. Therefore, we proposed a dual-frequency combination method for reflected signals to solve the problem of phase tracking under a high sea state [116]. The main equations of this proposed method are shown in Figure 12. The experimental results show that when the sea is relatively calm, the RMSE of derived sea levels is lower using the combination method than using single-frequency signals. Under a high sea state, the single-frequency method fails. However, when the combination method is used, the phase measurements are greatly recovered with a rough sea surface, and sea levels are determined with centimeter-level accuracy. Moreover, the proposed combination method enables the use of data with a higher elevation angle range than that in the traditional method using a single-frequency signal.

To evaluate the spatiotemporal resolution of a GNSS-R system like CYGNSS, a space-borne GNSS-R simulation was carried out in 2018 to analyze the distribution of the reflections. The results in Figure 13 show that when multi-GNSS satellites are available, the number of samples can be tripled compared with only using GPS, and the revisit time reaches approximately 3 h for L2 [63].

To sum up, the development of multi-frequency and multi-mode GNSS has afforded more opportunities and advantages for GNSS-R altimetry. First, the new signals (GPS L5) and new modulation mode (binary offset carrier modulation) perform better for sea level estimation than traditional L1 C/A with BPSK modulation. Second, sea level estimations from low elevation angles are less precise than those from high elevation angles; in other words, the elevation angle has a significant influence on sea level estimations. Because the elevation angle of a GEO satellite stays almost the same, sea level estimations retrieved from a GEO satellite are supposed to have more stable precision. The above-mentioned experiments do show that the precision of GEO results is better than that for IGSO or MEO satellite signals. Especially with the development of the Chinese BDS system, more GEO satellites have been successfully launched, thus affording more GNSS-R observation signals. Third, multi-frequency GNSS signals afford a combination of different signals to reduce

several altimetric errors and therefore improve the precision of sea level estimations, which has been verified for GNSS-IR in [29] and two-mode GNSS-R in [117].

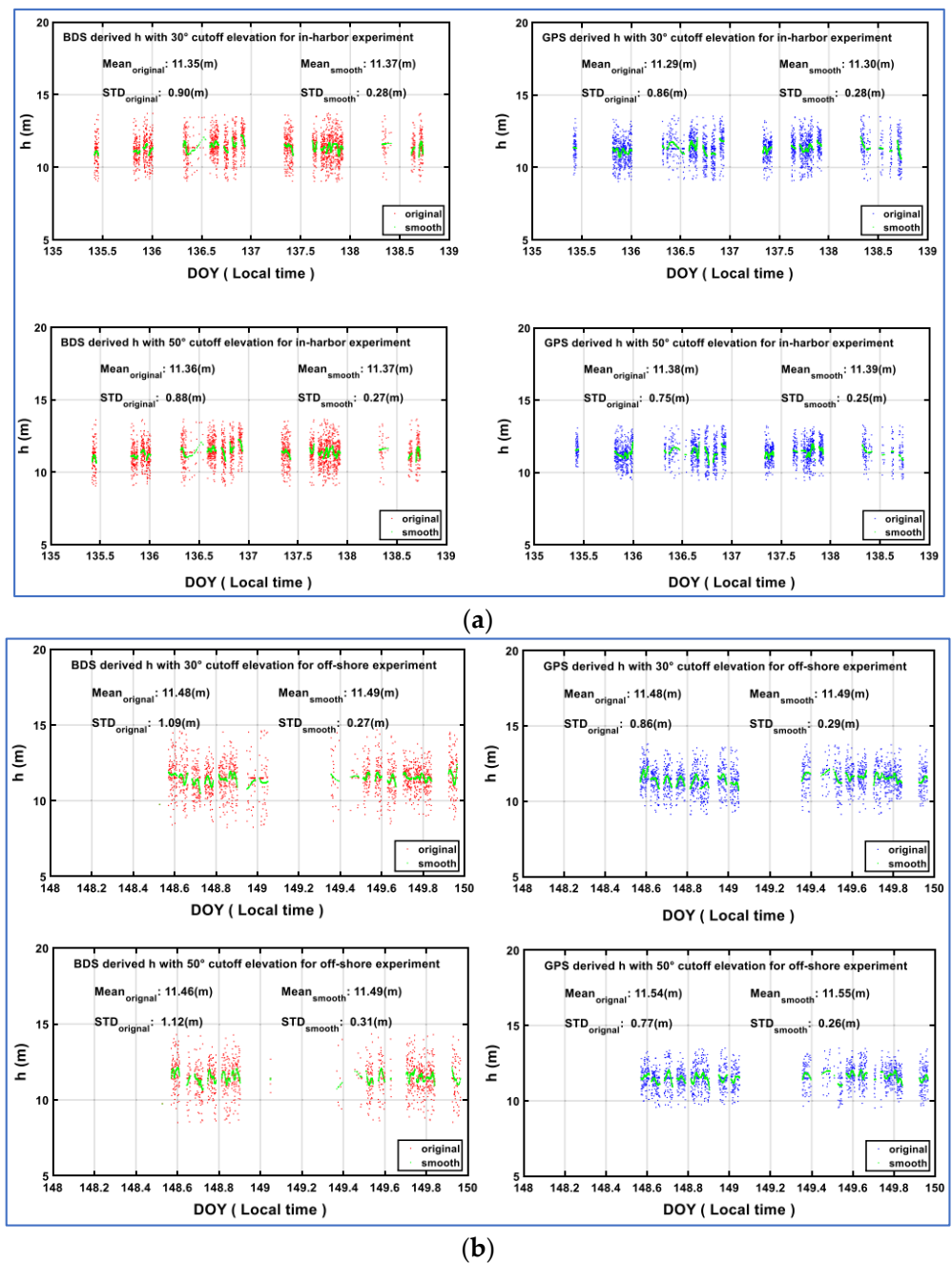


Figure 11. Reflector heights estimated from the (a) in-harbor and (b) off-shore ship-borne GNSS-R experiments as reported in [51].

- With rough sea surface:

$$\phi_{15}(t) = -a \tan 2\left(\frac{Q_{L15}}{I_{L15}}\right), \text{ where } \begin{cases} I_{L15} = I_{L1}I_{L5} + Q_{L1}Q_{L5} \\ Q_{L15} = Q_{L1}I_{L5} - I_{L1}Q_{L5} \end{cases}$$
- Under low sea states:

$$\phi_{15}(t) = \phi_1(t) + \psi_{L1} - (\phi_{L5}(t) + \psi_{L5}),$$
 with: $\phi_1(t) + \psi_{L1} = -a \tan 2\left(\frac{Q_{L1}}{I_{L1}}\right), \phi_{L5}(t) + \psi_{L5} = -a \tan 2\left(\frac{Q_{L5}}{I_{L5}}\right)$
- where I_{L_i}, Q_{L_i} ($for i = 1, 5$) are respective the in-phase and quadrature components of GNSS signal for frequency L1 and L5. ϕ_{15} is the phase of the combination between L1 and L5 signals.

Figure 12. Equations of the proposed phase combination method for GNSS-R altimetry referenced from [116].

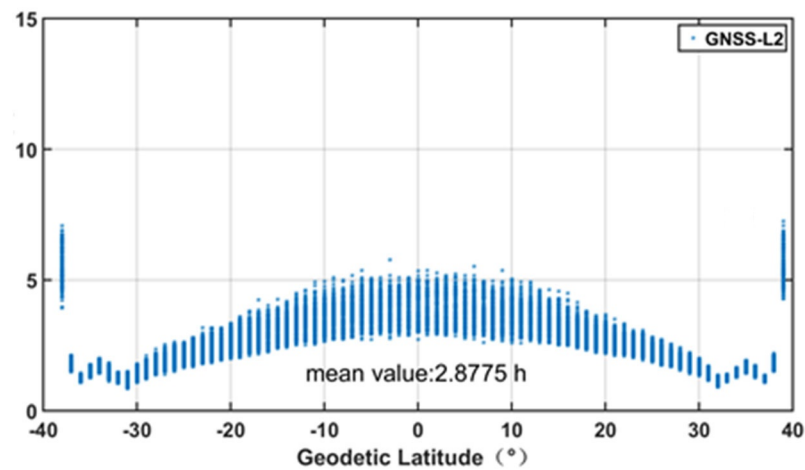


Figure 13. Mean revisit times for the four-system GNSS-R simulations at different latitudes during a single cycle at L2 frequencies as found in [63].

2.4. Current GNSS Networks and Satellite Constellations

After more than 30 years of development, GNSS-R-based sea level measurement has been widely used in many real circumstances. For example, the UK National Oceanography Centre (NOC) has developed a web portal for GNSS-IR global sea level data. GNSS development has made more and more signals with different frequencies available for estimating sea level. GPS, BDS, GLONASS, and Galileo are now all fully operative, providing three, eight, five, and five band signals, respectively. In addition to these global-scale navigation systems, some regional-scale navigation systems can be used to measure sea level. For example, the Satellite-Based Augmentation System (SBAS), QZSS, and Indian Regional Navigation Satellite System (IRNSS) can transmit two, four, and two band signals, respectively. Using multi-constellation and multi-frequency signals can give higher performance and thus better accuracy in measuring sea level. Spatiotemporal resolution can also be improved significantly. In general, a sea level estimation based on multi-constellation and multi-frequency signals considerably outperforms one based on a single-band signal. Because of the obvious benefits, future research will focus on combining multiple band signals and multiple GNSS constellations to improve sea level estimation accuracy.

Among these systems, the BDS of China started with the demonstration of the BeiDou navigation satellite system (BDS-1) in 2003 and the BeiDou regional navigation satellite system (BDS-2) in 2012, which evolved to BDS-3. Since July 2020, BDS-3 has completed constellation deployment and started to provide global services. BDS-2 satellites provide three public service signals, namely B1I, B2I, and B3I, and BDS-3 satellites provide five

public signals, namely B1I, B1C, B2a, B2b, and B3I. The multi-frequency signals and multi-orbits of the BDS system provide new opportunities for GNSS-R applications. By mid-June 2021, there were 49 operational BDS satellites in orbit. BDS-2 now consists of six satellites in GEO, seven satellites in IGSO, and three satellites in MEO. BDS-3 consists of 23 healthy MEO, 3 IGSO, and 2 GEO satellites. What is special about the extra IGSO and GEO satellites is that they have a relatively fixed activity range. Such a layout can enhance BDS accuracy in China and the Asia–Pacific region. The diversity of satellite orbits also increases the diversity of GNSS-R sea level observations; this is advantageous for estimating sea level accurately with a single-constellation GNSS signal. Sea level estimation based on multi-constellation and multi-frequency signals is not feasible in some circumstances owing to the high cost of receivers supporting the collection of such signals, although the receivers can perform better in GNSS-R-based sea level estimation. Therefore, using the diversity of BDS satellite signals to observe sea levels with high precision is also a future research topic. The diversity of BDS satellites will also bring more opportunities for GNSS-R altimetry than other GNSS satellite methods.

3. Future Developments

GNSS-R altimetry receivers have limited accuracy due to the narrow bandwidth of GNSS signals. As signals with new modulations and wider bandwidths become available, the next-generation receivers will be able to process more signals with excellent ranging, such as B1 and E5. For sea surface altimetry, higher digital quantization bits and sampling rates are conducive to accuracy. However, sampling rates are generally low because of hardware limitations. In the future, altimetry accuracy will be further improved with improvements in the receiver and GNSS-R algorithm.

GNSS-R constellations of CYGNSS have shown its powerful space–time observation ability for remote sensing. With the development of the Chinese FengYun series satellite for GNSS-R applications, more GNSS-R satellites will be successfully launched in the future. More GNSS-R observations will be combined to enhance sea surface altimetry. Improving the spatiotemporal resolution and accuracy of space-borne GNSS-R altimetry will still be a great challenge. Through reasonable and scientific antenna and orbit design, spatiotemporal resolution may become satisfactory with nano-satellite constellations. Improving path delay measurement accuracy requires studying high-precision ranging codes such as B2a/L5/E5. Better retracers are also important for recovering the geometry between the direct and reflected signals. The other method is to find a better index to improve the coherence of the reflected signals. The error models of space-borne altimetry should also be studied and established further.

With its improved accuracy and spatiotemporal resolution, space-borne GNSS-R altimetry can provide important scientific data for monitoring marine physical parameters such as mesoscale ocean eddies, the marine gravity field, global or regional ocean tide models, and ocean currents. Owing to the strong coherent reflection of ice sheets, space-borne GNSS-R altimetry can play an important role in polar observation and monitoring.

With the development of GNSS, the major countries of the world are constructing a new generation of satellite navigation systems to achieve higher accuracy, more reliable services, and more diverse applications. The unique constellation and signal advantages of LEO satellites have gradually attracted the attention and favor of the world's satellite navigation field, and they are expected to be a new step in developing the next generation of satellite navigation systems. Low-orbit satellites can enhance satellite navigation signals and enhance and supplement GNSS. They can also broadcast independent ranging signals through the integration of communication and navigation systems to form a backup positioning and navigation capability. They can provide more precise range signals with higher receiving power, as well as more precise satellite orbits, which will further improve the precision of future GNSS-R altimetry. This shows promise for realizing GNSS-R altimetry with high spatiotemporal resolution and high precision in the future.

4. Conclusions and Discussion

GNSS signals reflected from a sea surface have been demonstrated to retrieve sea surface height, and this GNSS-R ocean altimetry can supplement the traditional sea level monitoring method. GNSS-R altimetry still cannot meet the requirement of estimating sea levels with high precision and high spatiotemporal resolution. However, it will be possible to estimate sea levels in quasi-real time with high spatiotemporal resolution owing to the continuously increasing number of relevant stations and satellite systems. These include global GNSS stations and GNSS-R observation stations, as well as multi-mode and multi-frequency GNSS and regional augmentation satellite systems, including GPS, BDS, Galileo, GLONASS, SBAS, QZSS, and IRNSS. For GNSS-R altimetry, multi-mode and multi-frequency signals as well as their combinations can be used to correct altimetric errors such as inter-satellite deviation, inter-frequency deviation, ionospheric error, and tropospheric error to observe sea levels with high precision. Meanwhile, the development of low-cost GNSS receivers has enabled high-precision GNSS-R altimetry even using a mobile phone, which gives this technology a more promising future.

Because of their low cost, more space-borne GNSS-R missions can be expected in the near future, including single GNSS-R satellites and their constellations. Sea levels can be observed in more detail with high spatiotemporal resolution and a short revisit period. This will fulfill the need for mesoscale ocean observations in such research areas as global climate change, the global ocean gravity field, and the impact of sea level variations on human activities. Furthermore, advanced GNSS receivers and improved data processing algorithms will be studied to overcome the limitation of chip width and further improve the precision of space-borne GNSS-R altimetry. Therefore, GNSS-R altimetry will provide an alternative method for long-time sea level observations at the global and regional scales in the coming years.

Author Contributions: Idea proposal, conceptualization, project administration, funding acquisition, T.X.; investigation, data curation, writing—original draft preparation, writing—review and editing, N.W.; visualization, writing—original draft preparation, Y.H., Y.L., X.M. and F.G.; supervision, E.L.-B. All authors have read and agreed to the published version of the manuscript.

Funding: This research was partially funded by the National Natural Science Foundation of China, grant numbers 42192534; this research was partially funded by the Key Research and Development Program of Shandong Province (Major Technological Innovation Project), grant number 2021ZDSYS01; this research was partially funded by the National Natural Science Foundation of China, grant numbers 41931076, 41704017 and 41604003; and this research was partially funded by the National Natural Science Foundation of Shandong Province, grant number ZR2022MD046.

Data Availability Statement: The observation data used to support Figure 3 are available from SONEL "<https://www.sonel.org/spip.php?page=gps&idStation=4600> (accessed on 13 May 2024)". The data used to support Figure 2 are available from the corresponding author upon reasonable request. The images supporting Figure 9 are publicly available in the figshare repository, as part of this record [52]: "<https://www.mdpi.com/2072-4292/13/7/1378#> (accessed on 13 May 2024)". The Figure 10 data are publicly available as part of this record [120]: "<https://www.mdpi.com/2072-4292/13/22/4553#> (accessed on 13 May 2024)". The Figure 11 data are publicly available as part of this record [51]: "<https://link.springer.com/article/10.1007/s00190-020-01421-4> (accessed on 13 May 2024)". The Figure 13 data are publicly available as part of this record [63]: "<https://www.mdpi.com/2072-4292/10/1/67#> (accessed on 13 May 2024)".

Conflicts of Interest: The authors declare no conflicts of interest.

References

1. Cazenave, A.; Le, G.C. Sea level rise and its coastal impacts. *Earth's Future* **2013**, *2*, 15–34. [CrossRef]
2. Löfgren, J.S.; Haas, R.; Scherneck, H.G. Sea level time series and ocean tide analysis from multipath signals at five GPS sites in different parts of the world. *J. Geodyn.* **2014**, *80*, 66–80. [CrossRef]
3. Bouffard, J.; Roblou, L.; Birol, F.; Pascual, A.; Fenoglio-Marc, L.; Cancet, M.; Morrow, R.; Ménard, Y. Introduction and Assessment of Improved Coastal Altimetry Strategies: Case Study over the Northwestern Mediterranean Sea. In *Coastal Altimetry*; Vignudelli, S., Kostianoy, A.G., Cipollini, P., Benveniste, J., Eds.; Springer: Berlin/Heidelberg, Germany, 2011; pp. 297–330.

4. Roussel, N.; Ramillien, G.; Frappart, F.; Darrozes, J.; Gay, A.; Biancale, R.; Striebig, N.; Hanquiez, V.; Bertin, X.; Allain, D. Sea level monitoring and sea state estimate using a single geodetic receiver. *Remote Sens. Environ.* **2015**, *171*, 261–277. [[CrossRef](#)]
5. Larson, K.M.; Ray, R.D.; Williams, S.D.P. A 10-year comparison of water levels measured with a geodetic GPS receiver versus a conventional tide gauge. *J. Atmos. Ocean Technol.* **2017**, *34*, 295–307. [[CrossRef](#)]
6. Clarizia, M.P.; Ruf, C.S. Wind speed retrieval algorithm for the cyclone global navigation satellite system (CYGNSS) mission. *IEEE Trans. Geosci. Remote Sens.* **2016**, *54*, 4419–4432. [[CrossRef](#)]
7. Reinking, J.; Roggenbuck, O.; Even-Tzur, G. Estimating wave direction using terrestrial GNSS reflectometry. *Remote Sens.* **2019**, *11*, 1027. [[CrossRef](#)]
8. Larson, K.M.; Gutmann, E.D.; Zavorotny, V.U.; Braun, J.J.; Williams, M.W.; Nievinski, F.G. Can we measure snow depth with GPS receivers? *Geophys. Res. Lett.* **2009**, *36*, L17502. [[CrossRef](#)]
9. Tabibi, S.; Geremia-Nievinski, F.; Dam, T. Statistical comparison and combination of GPS, GLONASS, and multi-GNSS multipath reflectometry applied to snow depth retrieval. *IEEE Trans. Geosci. Remote Sens.* **2017**, *55*, 3773–3785. [[CrossRef](#)]
10. Larson, K.M.; Braun, J.J.; Small, E.E.; Zavorotny, V.U.; Gutmann, E.D.; Bilich, A.L. GPS multipath and its relation to near-surface soil moisture content. *IEEE J. Sel. Topics Appl. Earth Observ. Remote Sens.* **2010**, *3*, 91–99. [[CrossRef](#)]
11. Chew, C.C.; Small, E.E.; Larson, K.M.; Zavorotny, V.U. Effects of near-surface soil moisture on GPS SNR data: Development of a retrieval algorithm for soil moisture. *IEEE Trans. Geosci. Remote Sens.* **2014**, *52*, 537–543. [[CrossRef](#)]
12. Martín-Neira, M. A passive reflectometry and interferometry system (PARIS): Application to ocean altimetry. *ESA J.* **1993**, *17*, 331–355.
13. Martín-Neira, M.; Caparrini, M.; Font-Rossello, J.; Lannelongue, S.; Vallmitjana, C.S. The PARIS concept: An experimental demonstration of sea surface altimetry using GPS reflected signals. *IEEE Trans. Geosci. Remote Sens.* **2001**, *39*, 142–150. [[CrossRef](#)]
14. Lowe, S.; Zuffada, C.; Chao, Y.; Kroger, P.; Young, L.; LaBrecque, J. 5-cm-precision aircraft ocean altimetry using GPS reflections. *Geophys. Res. Lett.* **2002**, *29*, 13-1–13-4. [[CrossRef](#)]
15. Ruffini, G.; Soulat, F.; Caparrini, M.; Germain, O.; Martín-Neira, M. The eddy experiment: Accurate GNSS-R ocean altimetry from low altitude aircraft. *Geophys. Res. Lett.* **2004**, *31*, X-1–X-4. [[CrossRef](#)]
16. Löfgren, J.; Haas, R.; Scherneck, H.; Bos, M. Three months of local sea level derived from reflected GNSS signals. *Radio Sci.* **2011**, *46*, RS0C05. [[CrossRef](#)]
17. Semmling, A.; Beyerle, G.; Stosius, R.; Dick, G.; Wickert, J.; Fabra, F.; Cardellach, E.; Ribó, S.; Rius, A.; Helm, A.; et al. Detection of Arctic ocean tides using interferometric GNSS-R signals. *Geophys. Res. Lett.* **2011**, *38*, L04103. [[CrossRef](#)]
18. Rius, A.; Noque's-Correig, O.; Ribo, S.; Cardellach, E.; Oliveras, S.; Valencia, E.; Park, H.; Tarongí, J.M.; Camps, A.; Marel, H.; et al. Altimetry with GNSS-R interferometry: First proof of concept experiment. *GPS Solut.* **2012**, *16*, 231–241. [[CrossRef](#)]
19. Cardellach, E.; Li, W.; Rius, A.; Semmling, M.; Wickert, J.; Zus, F.; Christo, S.R.; Buontempo, C. First Precise Spaceborne Sea Surface Altimetry with GNSS Reflected Signals. *IEEE J. Sel. Top. Appl. Earth Obs. Remote Sens.* **2020**, *13*, 102–112. [[CrossRef](#)]
20. Yang, Y.; Mao, Y.; Sun, B. Basic performance and future developments of BeiDou global navigation satellite system. *Satell Navig.* **2020**, *1*, 1. [[CrossRef](#)]
21. Larson, K.M.; Ray, R.D.; Nievinski, F.G.; Freymueller, J.T. The accidental tide gauge: A GPS reflection case study from Kachemak Bay, Alaska. *IEEE Geosci. Remote Sens. Lett.* **2013**, *10*, 1200–1204. [[CrossRef](#)]
22. Anderson, K.D. Determination of water level and tides using interferometric observations of GPS signals. *J. Atmos. Ocean Technol.* **2000**, *17*, 1118–1127. [[CrossRef](#)]
23. Nievinski, F.G.; Larson, K.M. Inverse modeling of GPS multipath for snow depth estimation—Part I: Formulation and simulations. *IEEE Trans. Geosci. Remote Sens.* **2014**, *52*, 6555–6563. [[CrossRef](#)]
24. Strandberg, J.; Hobiger, T.; Haas, R. Improving GNSS-R sea level determination through inverse modeling of SNR data. *Radio Sci.* **2016**, *51*, 1286–1296. [[CrossRef](#)]
25. Strandberg, J.; Hobiger, T.; Haas, R. Real-time sea-level monitoring using Kalman filtering of GNSS-R data. *GPS Solut.* **2019**, *23*, 61. [[CrossRef](#)]
26. Rodriguez-Alvarez, N.; Bosch-Lluis, X.; Camps, A.; Ramos-Perez, I.; Valencia, E.; Park, H.; Vall-Ilossera, M. Water level monitoring using the interference pattern GNSS-R technique. In Proceedings of the IEEE International Geoscience and Remote Sensing Symposium (IGARSS), Vancouver, BC, Canada, 24–29 July 2011.
27. Wang, X.; Zhang, Q.; Zhang, S. Water levels measured with SNR using wavelet decomposition and Lomb-Scargle periodogram. *GPS Solut.* **2018**, *22*, 22. [[CrossRef](#)]
28. Wang, X.; Zhang, Q.; Zhang, S. Sea level estimation from SNR data of geodetic receivers using wavelet analysis. *GPS Solut.* **2019**, *23*, 6. [[CrossRef](#)]
29. Wang, X.; Zhang, Q. Evaluation and combination of quad-constellation multi-gnss multipath reflectometry applied to sea level retrieval. *Remote Sens. Environ. Interdiscip. J.* **2019**, *231*, 111229. [[CrossRef](#)]
30. Nievinski, F.G.; Larson, K.M. Forward modeling of GPS multipath for near-surface reflectometry and positioning applications. *GPS Solut.* **2014**, *18*, 309–322. [[CrossRef](#)]
31. Nievinski, F.G.; Larson, K.M. An open source GPS multipath simulator in Matlab/Octave. *GPS Solut.* **2014**, *18*, 473–481. [[CrossRef](#)]
32. Tabibi, S.; Geremia-Nievinski, F.; Francis, O.; Dam, T. Tidal analysis of GNSS Reflectometry applied for coastal sea level sensing in Antarctica and Greenland. *Remote Sens. Environ.* **2020**, *248*, 111959. [[CrossRef](#)]

33. Reinking, J. GNSS-SNR water level estimation using global optimization based on interval analysis. *J. Geod. Sci.* **2016**, *6*, 80–92. [[CrossRef](#)]
34. Jin, S.; Qian, X.; Wu, X. Sea level change from BeiDou Navigation Satellite System-Reflectometry (BDS-R): First results and evaluation. *Glob. Planet. Chang.* **2017**, *149*, 20–25. [[CrossRef](#)]
35. Wang, N.; Xu, T.; Gao, F.; Xu, G. Sea Level Estimation Based on GNSS Dual-Frequency Carrier Phase Linear Combinations and SNR. *Remote Sens.* **2018**, *10*, 470. [[CrossRef](#)]
36. Wang, N.; Wang, J.; Xu, T.; Gao, F.; He, Y.; Meng, X. Applications of ground-based multipath reflectometry based on combinations of pseudorange and carrier phase observations of multi-GNSS dual-frequency signals. *IEEE J. Sel. Top. Appl. Earth Obs. Remote Sens.* **2021**, *14*, 9557–9570. [[CrossRef](#)]
37. Wang, N.; Xu, T.; Gao, F.; He, Y.; Meng, X.; Jing, L.; Ning, B. Sea-Level Monitoring and Ocean Tide Analysis based on Multipath Reflectometry Using Received Strength Indicator Data from Multi-GNSS Signals. *IEEE Trans. Geosci. Remote Sens.* **2022**, *60*, 4211513. [[CrossRef](#)]
38. Liu, Q.; Zhang, S. An improved sea level retrieval method using the differential evolution of GNSS SNR data. *Adv. Space Res.* **2020**, *67*, 975–984. [[CrossRef](#)]
39. Li, Y.; Yu, K.; Jin, T.; Chang, X.; Wang, Q.; Li, J. Development of GNSS-IR instrument based on low-cost positioning chips and its performance evaluation for estimating reflective height variation. *GPS Solut.* **2021**, *25*, 1–12.
40. Williams, S.D.P.; Bell, P.S.; McCann, D.L.; Cooke, R.; Sams, C. Demonstrating the potential of low-cost GPS units for the remote measurement of tides and water levels using interferometric reflectometry. *J. Atmos. Ocean. Technol.* **2020**, *37*, 1925–1935. [[CrossRef](#)]
41. Strandberg, J.; Haas, R. Can we measure sea level with a tablet computer? *IEEE Geosci. Remote Sens. Lett.* **2019**, *17*, 1876–1878. [[CrossRef](#)]
42. Liu, Z.; Du, L.; Zhou, P.; Liu, Z.; Zhang, Z.; Xu, Z. Performance assessment of GNSS-IR altimetry using signal-to-noise ratio data from a Huawei P30 smartphone. *GPS Solut.* **2022**, *26*, 42. [[CrossRef](#)]
43. Fagundes, M.A.R.; Mendonça-Tinti, I.; Iescheck, A.L.; Akos, D.M.; Geremia-Nievinski, F. An open-source low-cost sensor for SNR-based GNSS reflectometry: Design and long-term validation towards sea-level altimetry. *GPS Solut.* **2021**, *25*, 73. [[CrossRef](#)]
44. Zavorotny, V.U.; Gleason, S.; Cardellach, E.; Camps, A. Tutorial on Remote Sensing Using GNSS Bistatic Radar of Opportunity. *Geosci. Remote Sens.* **2014**, *2*, 8–45. [[CrossRef](#)]
45. Garrison, J.L.; Katzberg, S.J.; Hill, M.I. Effect of sea roughness on bistatically scattered range coded signals from the Global Positioning System. *Geophys. Res. Lett.* **1998**, *25*, 2257–2260. [[CrossRef](#)]
46. Helm, A. Ground-based GPS altimetry with the L1 OpenGPS receiver using carrier phase delay observations of reflected GPS signals. Doctoral Dissertation, Deutsches GeoForschungsZentrum GFZ, Potsdam, Germany, 2008.
47. Lowe, S.T.; Meehan, T.; Young, L. Direct signal enhanced semicodeless processing of GNSS surface-reflected signals. *IEEE J. Sel. Top. Appl. Earth Obs. Remote Sens.* **2014**, *7*, 1469–1472. [[CrossRef](#)]
48. Carreno-Luengo, H.; Camps, A.; Ramos-Perez, I.; Rius, A. Experimental evaluation of GNSS-reflectometry altimetric precision using the P (Y) and C/A signals. *IEEE J. Sel. Top. Appl. Earth Obs. Remote Sens.* **2014**, *7*, 1493–1500. [[CrossRef](#)]
49. Treuhaft, R.N.; Lowe, S.T.; Zuffada, C.; Chao, Y. 2-cm GPS altimetry over Crater Lake. *Geophys. Res. Lett.* **2001**, *28*, 4343–4346. [[CrossRef](#)]
50. Zhang, Y.; Tian, L.; Meng, W.; Gu, Q.; Han, Y.; Hong, Z. Feasibility of Code-Level Altimetry Using Coastal BeiDou Reflection (BeiDou-R) Setups. *IEEE J. Sel. Top. Appl. Earth Obs. Remote Sens.* **2015**, *8*, 4130–4140. [[CrossRef](#)]
51. Gao, F.; Xu, T.; Wang, N.; He, Y.; Luo, X. A shipborne experiment using a dual-antenna reflectometry system for GPS/BDS code delay measurements. *J. Geodesy.* **2020**, *94*, 88. [[CrossRef](#)]
52. Gao, F.; Xu, T.; Meng, X.; Wang, N.; He, Y.; Ning, B. A Coastal Experiment for GNSS-R Code-Level Altimetry Using BDS-3 New Civil Signals. *Remote Sens.* **2021**, *13*, 1378. [[CrossRef](#)]
53. Wu, J.; Chen, Y.; Gao, F.; Guo, P.; Wang, X.; Niu, X.; Wu, M.; Fu, N. Sea surface estimation by ground-based BDS GEO satellit reflectometry. *IEEE J. Sel. Top. Appl. Earth Obs. Remote Sens.* **2020**, *13*, 5550–5559. [[CrossRef](#)]
54. Lowe, S.T.; Zuffada, C.; Labrecque, J.L.; Lough, M.; Young, L.E. An ocean-altimetry measurement using reflected GPS signals observed from a low-altitude aircraft. *IEEE Int. Geosci. Remote Sens. Symp.* **2000**, *5*, 2185–2187.
55. Semmling, A.M.; Beckheinrich, J.; Wickert, J.; Beyerle, G.; Schon, S.; Fabra, F.; Pflug, H.; He, K.; Schwabe, J.; Scheinert, M. Sea surface topography retrieved from GNSS reflectometry phase data of the GEOHALO flight mission. *Geophys. Res. Lett.* **2014**, *41*, 954–960. [[CrossRef](#)]
56. Mashburn, J.; Axelrad, P.; Lowe, S.T.; Larson, K.M. An assessment of the precision and accuracy of altimetry retrievals for a monterey bay GNSS-R experiment. *IEEE J. Sel. Top. Appl. Earth Obs. Remote Sens.* **2016**, *9*, 4660–4668. [[CrossRef](#)]
57. Zheng, W.; Li, Z.; Wu, F. Research progress in improving the accuracy of underwater inertial/gravity integrated navigation based on the new generation of GNSS-R constellation sea surface altimetry principle. *Sci. Technol. Eng.* **2019**, *19*, 21–36.
58. Carreno-Luengo, H.; Camps, A.; Ruf, C.; Floury, N.; Martín-Neira, M.; Wang, T.; Khalsa, S.J.; Clarizia, M.P.; Reynolds, J.; Johnson, J.; et al. The IEEE-SA Working Group on Spaceborne GNSS-R: Scene Study. *IEEE Access* **2021**, *9*, 89906–89933. [[CrossRef](#)]
59. Hoseini, M.; Asgarimehr, M.; Zavorotny, V.; Nahavandchi, H.; Ruf, C.; Wickert, J. First Evidence of Mesoscale Ocean Eddies Signature in GNSS Reflectometry Measurements. *Remote Sens.* **2020**, *12*, 542. [[CrossRef](#)]

60. Peng, Q.; Jin, S. Significant Wave Height Estimation from Space-Borne Cyclone-GNSS Reflectometry. *Remote Sens.* **2019**, *11*, 584. [[CrossRef](#)]
61. Wang, Y.; Morton, Y.J. Ionospheric Total Electron Content and Disturbance Observations from Space-Borne Coherent GNSS-R Measurements. *IEEE Trans. Geosci. Remote Sens.* **2022**, *60*, 5801013. [[CrossRef](#)]
62. Bai, W.; Zhao, D.; Xia, J.; Sun, Y.; Du, Q.; Wang, X.; Meng, X.; Liu, C.; Cai, Y.; Wang, Y. Statistical Analysis of Simulated Space-Borne GNSS-R Data in Different Antenna Coverage and Installation Condition. *Geomat. Inf. Sci. Wuhan Univ.* **2023**, *48*, 386–395.
63. Gao, F.; Xu, T.; Wang, N.; Jiang, C.; Du, Y.; Nie, W.; Xu, G. Spatiotemporal Evaluation of GNSS-R Based on Future Fully Operational Global Multi-GNSS and Eight-LEO Constellations. *Remote Sens.* **2018**, *10*, 67. [[CrossRef](#)]
64. Gleason, S.; Gommenginger, C.; Cromwell, D. Fading statistics and sensing accuracy of ocean scattered GNSS and altimetry signals. *Adv. Space Res.* **2010**, *46*, 208–220. [[CrossRef](#)]
65. Pascual, D.; Camps, A.; Martín, F.; Park, H.; Arroyo, A.A.; Onrubia, R. Precision Bounds in GNSS-R Ocean Altimetry. *IEEE J. Sel. Top. Appl. Earth Obs. Remote Sens.* **2014**, *7*, 1416–1423. [[CrossRef](#)]
66. Clarizia, M.P.; Ruf, C.; Cipollini, P.; Zuffada, C. First spaceborne observation of sea surface height using GPS-Reflectometry. *Geophys. Res. Lett.* **2016**, *43*, 767–774. [[CrossRef](#)]
67. D’Addio, S.; Martín-Neira, M.; Bisceglie, M.; Galdi, C.; Alemany, F.M. GNSS-R Altimeter Based on Doppler Multi-looking. *IEEE J. Sel. Top. Appl. Earth Obs. Remote Sens.* **2014**, *7*, 1452–1460. [[CrossRef](#)]
68. Carreno-Luengo, H.; Camps, A.; Via, P.; Muñoz, J.F.; Cortiella, A.; Vidal, D.; Jané, J.; Catarino, N.; Hagenfeldt, M.; Palomo, P.; et al. 3Cat-2—An experimental nanosatellite for GNSS-R earth observation: Mission concept and analysis. *IEEE J. Sel. Top. Appl. Earth Obs. Remote Sens.* **2016**, *9*, 4540–4551. [[CrossRef](#)]
69. Camps, A.; Park, H.; Domènech, E.V.; Pascual, D.; Martín, F.; Rius, A.; Ribo, S.; Benito, J.; Saameno, P.; Staton, G.; et al. Optimization and Performance Analysis of Interferometric GNSS-R Altimeters: Application to the PARIS IoD Mission. *IEEE J. Sel. Top. Appl. Earth Obs. Remote Sens.* **2014**, *7*, 1436–1451. [[CrossRef](#)]
70. Wickert, J.; Cardellach, E.; Martín-Neira, M.; Bandeiras, J.; Bertino, L.; Andersen, O.B.; Camps, A.; Catarino, N.; Chapron, B.; Fabra, F.; et al. Geros-ISS: GNSS Reflectometry, Radio Occultation, and Scatterometry Onboard the International Space Station. *IEEE J. Sel. Top. Appl. Earth Obs. Remote Sens.* **2016**, *9*, 4552–4581. [[CrossRef](#)]
71. Unwin, M.J.; Pierdicca, N.; Cardellach, E.; Rautiainen, K.; Foti, G.; Blunt, P.; Guerriero, L.; Santi, E.; Tossaint, M. An Introduction to the HydroGNSS GNSS Reflectometry Remote Sensing Mission. *IEEE J. Sel. Top. Appl. Earth Obs. Remote Sens.* **2021**, *14*, 6987–6999. [[CrossRef](#)]
72. Chen, C.; Wang, X.; Bian, Z.; Wei, H.; Fan, D.; Bai, Z. Improving GNSS-R Ocean Wind Speed Retrieval for the BF-1 Mission Using Satellite Platform Attitude Measurements. *IEEE J. Sel. Top. Appl. Earth Obs. Remote Sens.* **2023**, *16*, 2121–2133. [[CrossRef](#)]
73. Wang, F.; Li, J.; Yang, D.; Zheng, Q.; Li, F. Wind Speed Retrieval and Assessment Using GNSS-R Data from “Jilin 1” Kuanfu 01B Satellite. *Geomat. Inf. Sci. Wuhan Univ.* **2023**, *49*, 56–67.
74. Mashburn, J.; Axelrad, P.; Lowe, S.T.; Larson, K.M. Global Ocean Altimetry with GNSS Reflections from TechDemoSat-1. *IEEE Trans. Geosci. Remote Sens.* **2018**, *56*, 4088–4097. [[CrossRef](#)]
75. Rius, A.; Cardellach, E.; Fabra, F.; Li, W.; Ribó, S.; Hernández-Pajares, M. Feasibility of GNSS-R Ice Sheet Altimetry in Greenland Using TDS-1. *Remote Sens.* **2017**, *9*, 742. [[CrossRef](#)]
76. Cartwright, J.; Clarizia, M.P.; Cipollini, P.; Banks, C.J.; Srokosz, M. Independent DEM of Antarctica Using GNSS-R Data from TechDemoSat-1. *Geophys. Res. Lett.* **2018**, *45*, 6117–6123. [[CrossRef](#)]
77. Cartwright, J.; Banks, C.J.; Srokosz, M. Improved GNSS-R bi-static altimetry and independent digital elevation models of Greenland and Antarctica from TechDemoSat-1. *Cryosphere* **2020**, *14*, 1909–1917. [[CrossRef](#)]
78. Li, W.; Rius, A.; Fabra, F.; Martín-Neira, M.; Cardellach, E.; Ribó, S.; Yang, D. The Impact of Inter-Modulation Components on Interferometric GNSS-Reflectometry. *Remote Sens.* **2016**, *8*, 1013. [[CrossRef](#)]
79. Li, W.; Cardellach, E.; Fabra, F.; Ribo, S.; Rius, A. Assessment of Spaceborne GNSS-R Ocean Altimetry Performance Using CYGNSS Mission Raw Data. *IEEE Trans. Geosci. Remote Sens.* **2020**, *58*, 238–250. [[CrossRef](#)]
80. Li, W.; Cardellach, E.; Ribó, S.; Rius, A.; Zhou, B. First spaceborne demonstration of BeiDou-3 signals for GNSS reflectometry from CYGNSS constellation. *Chin. J. Aeronaut.* **2021**, *34*, 1–10. [[CrossRef](#)]
81. Zhang, Y.; Ma, D.; Meng, W.; Zheng, Q.; Yang, S. Sea surface height inversion of GPS reflected signal based on TechDemoSat-1 satellite. *J. Beijing Univ. Aeronaut. Astronaut.* **2021**, *47*, 1941–1948.
82. Cardellach, E.; Ao, C.O.; Juárez, M.T.; Hajj, G.A. Carrier phase delay altimetry with GPS-reflection/occultation interferometry from low Earth orbiters. *Geophys. Res. Lett.* **2004**, *31*, L10402. [[CrossRef](#)]
83. Semmling, A.M.; Leister, V.; Saynisch, J.; Zus, F.; Heise, S.; Wickert, J. A Phase-Altmetric Simulator: Studying the Sensitivity of Earth-Reflected GNSS Signals to Ocean Topography. *IEEE Trans. Geosci. Remote Sens.* **2016**, *54*, 6791–6802. [[CrossRef](#)]
84. Li, W.; Cardellach, E.; Fabra, F.; Ribó, S.; Rius, A. Lake Level and Surface Topography Measured with Spaceborne GNSS-Reflectometry from CYGNSS Mission: Example for the Lake Qinghai. *Geophys. Res. Lett.* **2018**, *45*, 13332–13341. [[CrossRef](#)]
85. Wang, Y.; Morton, Y.J. Coherent GNSS Reflection Signal Processing for High-Precision and High-Resolution Spaceborne Applications. *IEEE Trans. Geosci. Remote Sens.* **2021**, *59*, 831–842. [[CrossRef](#)]
86. Wang, Y.; Morton, Y.J. River Slope Observation from Spaceborne GNSS-R Carrier Phase Measurements: A Case Study. *IEEE Geosci. Remote Sens. Lett.* **2022**, *19*, 1503105. [[CrossRef](#)]

87. Nguyen, V.A.; Nogués-Correig, O.; Yuasa, T.; Masters, D.; Irisov, V. Initial GNSS Phase Altimetry Measurements from the Spire Satellite Constellation. *Geophys. Res. Lett.* **2020**, *47*, e2020GL088308. [[CrossRef](#)]
88. Roesler, C.J.; Morton, Y.J.; Wang, Y.; Nerem, R.S. Coherent GNSS-Reflections Characterization Over Ocean and Sea Ice Based on Spire Global CubeSat Data. *IEEE Trans. Geosci. Remote Sens.* **2022**, *60*, 5801918. [[CrossRef](#)]
89. Nogués-Correig, O.; Galí, E.C.; Campderrós, J.S.; Rius, A. A GPS-reflections receiver that computes Doppler/delay maps in real time. *IEEE Trans. Geosci. Remote Sens.* **2006**, *45*, 156–174. [[CrossRef](#)]
90. Rius, A.; Fabra, F.; Ribo, S.; Arco, J.C.; Oliveras, S.; Cardellach, E.; Camps, A.; Nogués-Correig, O.; Kainulainen, J.; Rohue, E.; et al. PARIS interferometric technique proof of concept: Sea surface altimetry measurements. In Proceedings of the IEEE International Geoscience and Remote Sensing Symposium (IGARSS), Munich, Germany, 22–27 July 2012.
91. Helm, A.; Montenbruck, O.; Ashjaee, J.; Yudanov, S.; Beyerle, G.; Stosius, R.; Rothacher, M. GORS-A GNSS Occultation, Reflectometry and Scatterometry Space Receiver. In Proceedings of the 20th International Technical Meeting of the Satellite Division of the Institute of Navigation (ION GNSS 2007), Fort Worth, TX, USA, 25–28 September 2007.
92. Jing, C.; Niu, X.; Duan, C.; Lu, F.; Di, G.; Yang, X. Sea surface wind speed retrieval from the first Chinese GNSS-R mission: Technique and preliminary results. *Remote Sens.* **2019**, *11*, 3013. [[CrossRef](#)]
93. Guo, Z.; Liu, B.; Wan, W.; Lu, F.; Niu, X.; Ji, R.; Jing, C.; Li, W.; Chen, X.; Yang, J.; et al. Soil moisture retrieval using BuFeng-1 A/B based on land surface clustering algorithm. *IEEE J. Sel. Top. Appl. Earth Obs. Remote Sens.* **2022**, *15*, 4680–4689. [[CrossRef](#)]
94. Sun, Y.; Liu, C.; Du, Q.; Wang, X.; Bai, W.; Kirchengast, G.; Xia, J.; Meng, X.; Wang, D.; Cai, Y.; et al. Global navigation satellite system occultation sounder II (GNOS II). In Proceedings of the IEEE International Geoscience and Remote Sensing Symposium (IGARSS), Fort Worth, TX, USA, 23–28 July 2017.
95. Huang, F.; Xia, J.; Yin, C.; Zhai, X.; Yang, G.; Bai, W.; Sun, Y.; Du, Q.; Wang, X.; Qiu, T.; et al. Spaceborne GNSS Reflectometry with Galileo Signals on FY-3E/GNOS-II: Measurements, Calibration, and Wind Speed Retrieval. *IEEE Geosci. Remote Sens. Lett.* **2023**, *20*, 3501505. [[CrossRef](#)]
96. Onrubia, R.; Pascual, D.; Querol, J.; Park, H.; Camps, A. The global navigation satellite systems reflectometry (GNSS-R) microwave interferometric reflectometer: Hardware, calibration, and validation experiments. *Sensors* **2019**, *19*, 1019. [[CrossRef](#)]
97. Munoz-Martin, J.F.; Miguelez, N.; Castella, R.; Fernandez, L.; Solanellas, A.; Via, P.; Camps, A. 3Cat-4: Combined GNSS-R, L-Band radiometer with RFI mitigation, and AIS receiver for an I-Unit Cubesat based on software defined radio. In Proceedings of the IEEE International Geoscience and Remote Sensing Symposium (IGARSS), Valencia, Spain, 22–27 July 2018.
98. Caparrini, M.; Egido, A.; Soulat, F.; Germain, O.; Farres, E.; Dunne, S.; Ruffini, G. Oceanpal[®]: Monitoring sea state with a GNSS-R coastal instrument. In Proceedings of the IEEE International Geoscience and Remote Sensing Symposium (IGARSS), Barcelona, Spain, 23–28 July 2007.
99. Yang, D.K.; Zhang, Y.G.; Zhang, Q.S.; Li, Z.W. Airborne ocean wind-field retrieval system based on GPS scattering signals. *Acta Aeronaut. Astronaut. Sin.* **2006**, *27*, 310–313.
100. Hobiger, T.; Haas, R.; Löfgren, J.S. GLONASS-R: GNSS reflectometry with a frequency division multiple access-based satellite navigation system. *Radio Sci.* **2014**, *49*, 271–282. [[CrossRef](#)]
101. Ribó, S.; Arco-Fernández, J.C.; Cardellach, E.; Fabra, F.; Li, W.; Nogués-Correig, O.; Martín-Neira, M. A software-defined GNSS reflectometry recording receiver with wide-bandwidth, multi-band capability and digital beam-forming. *Remote Sens.* **2017**, *9*, 450. [[CrossRef](#)]
102. Lestarquit, L.; Peyrezabes, M.; Darrozes, J.; Motte, E.; Roussel, N.; Wautelet, G.; Frappart, F.; Ramillien, G.; Biancale, R.; Zribi, M. Reflectometry with an open-source software GNSS receiver: Use case with carrier phase altimetry. *IEEE J. Sel. Top. Appl. Earth Obs. Remote Sens.* **2016**, *9*, 4843–4853. [[CrossRef](#)]
103. Munoz-Martin, J.F.; Capon, L.F.; Ruiz-de-Azua, J.A.; Camps, A. The flexible microwave payload-2: A SDR-based GNSS-reflectometer and L-band radiometer for CubeSats. *IEEE J. Sel. Top. Appl. Earth Obs. Remote Sens.* **2020**, *13*, 1298–1311. [[CrossRef](#)]
104. Guruprasad, S. FPGA-Based GNSS Receiver Design for Reflectometry Applications. Ph.D. Thesis, York University, Toronto, ON, Canada, 2023.
105. Kurum, M.; Farhad, M.M.; Gurbuz, A.C. Integration of smartphones into small unmanned aircraft systems to sense water in soil by using reflected GPS signals. *IEEE J. Sel. Top. Appl. Earth Obs. Remote Sens.* **2020**, *14*, 1048–1059. [[CrossRef](#)]
106. Farhad, M.M.; Kurum, M.; Gurbuz, A.C. A Ubiquitous GNSS-R Methodology to Estimate Surface Reflectivity Using Spinning Smartphone Onboard a Small UAS. *IEEE J. Sel. Top. Appl. Earth Obs. Remote Sens.* **2023**, *16*, 6568–6578. [[CrossRef](#)]
107. Martín-Neira, M.; D’Addio, S.; Buck, C.; Floury, N.; Prieto-Cerdeira, R. The PARIS ocean altimeter in-orbit demonstrator. *IEEE Trans. Geosci. Remote Sens.* **2011**, *49*, 2209–2237. [[CrossRef](#)]
108. Cardellach, E.; Wickert, J.; Baggen, R.; Benito, J.; Camps, A.; Catarino, N.; Chapron, B.; Dielacher, A.; Fabra, F.; Flato, G.; et al. GNSS transpolar earth reflectometry exploratory system (G-TERN): Mission concept. *IEEE Access* **2018**, *6*, 13980–14018. [[CrossRef](#)]
109. Martín-Neira, M.; Li, W.; Andres-Beivide, A.; Ballesteros-Sels, X. Cookie: A satellite concept for GNSS remote sensing constellations. *IEEE J. Sel. Topics Appl. Earth Observ. Remote Sens.* **2016**, *9*, 4593–4610. [[CrossRef](#)]
110. Rius, A.; Cardellach, E.; Martín-Neira, M. Altimetric analysis of the sea surface GPS reflected signals. *IEEE Trans. Geosci. Remote Sens.* **2010**, *48*, 2119–2127. [[CrossRef](#)]
111. Park, H.; Valencia, E.; Camps, A.; Rius, A.; Ribo, S.; Martín-Neira, M. Delay tracking in spaceborne GNSS-R ocean altimetry. *IEEE Geosci. Remote Sens. Lett.* **2013**, *10*, 57–61. [[CrossRef](#)]

112. Park, H.; Pascual, D.; Camps, A.; Martín, F.; Alonso-Arroyo, A.; Carreno-Luengo, H. Analysis of spaceborne GNSS-R delay-Doppler tracking. *IEEE J. Sel. Topics Appl.* **2017**, *7*, 1481–1492. [[CrossRef](#)]
113. Cardellach, E.; Rius, A.; Martín-Neira, M.; Fabra, F.; Nogues-Correig, O.; Ribo, S.; Kainulainen, J.; Camps, A.; D’Addio, S. Consolidating the precision of interferometric GNSS-R ocean altimetry using airborne experimental data. *IEEE Trans. Geosci. Remote Sens.* **2014**, *52*, 4992–5004. [[CrossRef](#)]
114. Fabra, F.; Cardellach, E.; Ribó, S.; Li, W.; Rius, A.; Arco-Fernández, J.; Nogués-Correig, O.; Praks, J.; Rouhe, E.; Seppänen, J.; et al. Is accurate synoptic altimetry achievable by means of interferometric GNSS-R? *Remote Sens.* **2019**, *11*, 505. [[CrossRef](#)]
115. Li, W.; Yang, D.; D’Addio, S.; Martín-Neira, M. Partial interferometric processing of reflected GNSS signals for ocean altimetry. *IEEE Geosci. Remote Sens. Lett.* **2014**, *11*, 1509–1513.
116. He, Y.; Gao, F.; Xu, T.; Meng, X.; Wang, N.; Ning, B. Coastal GNSS-R phase altimetry based on the combination of L1 and L5 signals under high sea states. *J. Geod.* **2023**, *97*, 19. [[CrossRef](#)]
117. Wang, N.; He, K.; Gao, F.; Chu, T.; Hou, J.; Xu, T. Analysis of GNSS-R Code-Level Altimetry using QZSS C/A, L1C, and BDS B1C signals and their Combinations in a Coastal Experiment. *IEEE J. Sel. Top. Appl. Earth Obs. Remote Sens.* **2023**, *16*, 4549–4564. [[CrossRef](#)]
118. Wang, N.; Gao, F.; Kong, Y.; Xu, T.; Jing, L.; Yang, L.; He, Y.; Yang, W.; Meng, X.; Ning, B. Soil Moisture Estimation Based on GNSS-R Using L5 Signals From a Quasi-Zenith Satellite System. *IEEE Geosci. Remote Sens. Lett.* **2022**, *19*, 2505005. [[CrossRef](#)]
119. Meng, X.; Gao, F.; Xu, T.; He, Y.; Wang, N.; Ning, B. Design of realtime GNSS-R software-defined receiver for coastal altimetry using GPS/BDS/QZSS signals. *GPS Solut.* **2024**, *28*, 20. [[CrossRef](#)]
120. He, Y.; Xu, T.; Gao, F.; Wang, N.; Meng, X.; Ning, B. Analysis and Mitigation of Crosstalk Effect on Coastal GNSS-R Code-Level Altimetry Using L5 Signals from QZSS GEO. *Remote Sens.* **2021**, *13*, 4553. [[CrossRef](#)]
121. Ning, B.; Wang, N.; Jing, L.; Gao, F.; Kong, Y.; He, Y. Research on the retrieval model of shore-based GNSS-R code altimetry. *J. Beijing Univ. Aeronaut. Astronaut.* **2023**.
122. He, Y.; Gao, F.; Xu, T.; Meng, X.; Wang, N. Coastal Altimetry Using Interferometric Phase from GEO Satellite in Quasi-Zenith Satellite System. *IEEE Geosci. Remote Sens. Lett.* **2022**, *19*, 3002505. [[CrossRef](#)]

Disclaimer/Publisher’s Note: The statements, opinions and data contained in all publications are solely those of the individual author(s) and contributor(s) and not of MDPI and/or the editor(s). MDPI and/or the editor(s) disclaim responsibility for any injury to people or property resulting from any ideas, methods, instructions or products referred to in the content.